

Theoretical studies on off-axis phase diagrams and Knight shifts in UTe_2 —Tetra-critical point, d-vector rotation, and multiple phases—

Kazushige Machida

Department of Physics, Ritsumeikan University, Kusatsu 525-8577, Japan

(Dated: May 6, 2024)

Inspired by recent remarkable sets of experiments on UTe_2 : discoveries of the fourth horizontal internal transition line running toward a tetra-critical point (TCP) at $H=15\text{T}$, the off-axis high field phases, and abnormally large Knight shift (KS) drop below T_c for $H\parallel a$ -magnetic easy axis, we advance further our theoretical work on the field (H)-temperature (T) phase diagram for $H\parallel b$ -magnetic hard axis which contains a positive sloped H_{c2} departing from TCP. A nonunitary spin-triplet pairing with three components explains these experimental facts simultaneously and consistently by assuming that the underlying normal electron system with a narrow bandwidth characteristic to the Kondo temperature $\sim 60\text{K}$ unsurprisingly breaks the particle-hole symmetry. This causes a special invariant term in Ginzburg-Landau (GL) free energy functional which couples directly with the 5f magnetic system, giving rise to the T_c splitting and ultimately to the positive sloped H_{c2} and the horizontal internal transition line connected to TCP. The large KS drop can be understood in terms of this GL invariance whose coefficient is negative and leads to a diamagnetic response where the Cooper pair spin is antiparallel to the applied field direction. The present scenario also accounts for the observed d-vector rotation phenomena and off-axis phase diagrams with extremely high $H_{c2}\gtrsim 70\text{T}$ found at angles in between the b and c -axes and between the bc plane and a -axis, making UTe_2 a fertile playground for a topological superconductor.

PACS numbers:

I. INTRODUCTION

Much attention has been focused on the recently found heavy Fermion superconductor UTe_2 ¹⁻⁴. Since the upper critical fields H_{c2} for the principal directions all surpass the Pauli paramagnetic limiting field, it is regarded as a prime candidate for a spin-triplet superconductor that is quite rare in nature except for UPt_3 ⁵⁻¹⁰, UBe_{13} ¹¹⁻¹³ and its Th-doped materials¹⁴⁻¹⁶ among abundant candidate materials. In these superconductors, the phase diagrams of the field (H) and temperature (T) plane consists of multiple distinctive phases. This is a hallmark of a triplet pairing because of its rich internal degrees of freedom associated with the spin and orbital spaces in the pairing function. This is exemplified by the textbook case of the p-wave superfluid ³He where the phase diagram in the T vs P (pressure) plane is divided into the ABM (A) and BW (B) phases¹⁷. Thus investigating the phase diagram in UTe_2 may be a fruitful route to identify the pairing symmetry realized.

UTe_2 has been discovered by Ran et al¹ in 2019 with its transition temperature $T_c = 1.6\text{K}$. Since then, there are a variety of experimental and theoretical works devoted to uncovering the realized Cooper pair symmetry^{3,4}. The system belongs to the so-called heavy Fermion materials in general with the enhanced electron effective mass and the Kondo coherent temperature $\sim 30\text{K}$. Initially it was thought that because of various similar physical properties it is a sister compound of the ferromagnetic superconductors UGe_2 , URhGe , and UCoGe , but no static long-ranged ferromagnetic order has been found. Instead, antiferromagnetic spin fluctuations are discovered¹⁸⁻²⁰. As for the pairing symmetry^{3,4}, (A) the spin triplet pairing

may be realized because of the Knight shift experiments showing the drop (unchanged) of the spin susceptibilities for $H \parallel b$ and c -axes (a -axis). (B) The time reversal symmetry is broken. (C) The chiral current on a sample edge is found. (D) The point nodes are oriented to the a -axis.

Since these experiments were mainly done by using $T_c = 1.6\text{K}$ samples, experiments using the new generation samples with $T_c = 2.1\text{K}$ challenge some of these conclusions. We are warned that some of the experimental facts are robust against sample quality, but some of the conclusions may be changed. For example, the overall structure of the phase diagram in the H - T plane for $H \parallel b$ -axis with the field-reinforced positive sloped H_{c2} is hardly changed. However, we need to further refine the important details of the existing phase diagram to narrow down the possible pairing symmetry in UTe_2 .

According to the recent report by Sakai et al²¹ by using the new generation high-quality samples with $T_c=2.1\text{K}$ ²², the three transition lines in the H - T phase diagram ($H\parallel b$ -axis) meet at a point of $H=15\text{T}$ comprising a tetra-critical point (TCP). This newly found fourth horizontal internal line runs almost parallel to the T -axis. Together with the previous discovery of the double transition in the specific heat measurement²³ corresponding to another two transition lines, it is understood that at least three phases exist in the H - T plane. These experimental facts encourage us to further investigate this material with the high possibility of a spin-triplet pairing state realized. In particular, we are urged to reproduce this characteristic H - T phase diagram with an appropriate pairing state, which could narrow down the possible pairing symmetry.

Here we put forth further our theoretical work²⁴⁻²⁸ in the light of the above new experimental facts and re-

produce the renewed phase diagrams with the horizontal fourth transition line for $H \parallel b$ -axis²¹ and extremely high H_{c2} for off-axis directions²⁹. We also develop our thoughts based on the nonunitary triplet scenario to explain the revised Knight shift (KS) experiments³⁰ by using the high-quality samples with $T_c=2.1\text{K}$ together with the previous NMR results³¹⁻³⁶. They show that KS decreases below T_c for all three directions; a , b , and c -axes. At first sight, this surprising result may be taken as a signature either for a spin singlet pairing or for the B phase-like state in the superfluid ^3He ¹⁷ where the d-vector has simultaneously the three components, making KS decrease in all directions. In this paper, we argue that neither spin singlet scenario nor the B phase-like state can consistently and coherently explain various compiled experimental facts which are summarized as follows:

(1) In the H - T plane for $H \parallel b$ -axis, the intermediate phase (MSC) is sandwiched between the low phase (LSC) and high field phase (HSC) at 15T ^{21,35}. The phase boundary of LSC-MSC comprises the fourth horizontal internal line ending at TCP. And $H_{c2}^b(T)$ has an unusual positive slope above 15T starting from TCP, namely $dH_{c2}^b/dT > 0$.

(2) MSC is characterized by the flux flow state²¹ in the H - T plane for $H \parallel b$ -axis. The vortices in MSC are easily depinned under external currents, suggesting that an exotic vortex lattice is formed in this field region around 15T , which coincides with the region where the d-vector is rotating mentioned below.

(3) The highest upper critical field H_{c2} occurs at narrow angle regions centered at $\theta = 35^\circ$ measured from the b -axis toward the c -axis³⁷⁻⁴⁰, and at $\phi \sim 10^\circ$ measured from the bc -plane toward the a -axis²⁹, reaching a surprisingly large value of more than 60T compared with $T_c=1.6\text{K}\sim 2.1\text{K}$. This high field region appears just above the meta-magnetic transition H_m . This phenomenon is similar to, but distinctive from the so-called reentrant superconducting phase observed in the sister compound URhGe, which appears in more wider angle region⁴¹⁻⁴³. For $H \parallel b$ -axis $H_{c2}^b(T)$ abruptly stops at $H_m(\parallel b) = 35\text{T}$.

(4) In KS by the ¹²⁵Te-NMR experiments, the decrease ΔK_a along the a -axis is extremely large³⁰ compared with the other two for the b -axis and c -axis, which are comparable, namely $|\Delta K_a| \gg |\Delta K_b| \sim |\Delta K_c|$ ³¹⁻³⁶. Since for the B phase^{17,44} in ^3He all three KS values are equal, corresponding to the spin susceptibility $\chi_a = \chi_b = \chi_c = -\frac{2}{3}\chi_N$ with χ_N the Pauli spin susceptibility in the normal state. The KS data are different from this fact and also from the spin-singlet state where $\chi_a = \chi_b = \chi_c = -\chi_N$.

(5) According to the NMR experiments^{32,33} on the $T_c=1.6\text{K}$ samples, with increasing $H \parallel b$ ($\parallel c$) the decrease of KS gradually diminishes, recovering to the normal χ_N value. This starts from 5T (a few T) and ends at 15T (5T) above which the decrease of KS ceases completely. Namely, the d-vector gradually rotates from the parallel direction to the perpendicular direction relative to the external field.

(6) Under pressure, the truly multiple phases⁴⁵⁻⁵¹ are observed and systematically evolving both as a function of

P and the field orientation. In particular, for $H \parallel a$ -axis the phase diagram consists of more than three phases, showing that the order parameters must be three components.

(7) There exist several important experiments to show the unconventional nature of the pairing symmetry⁵². This includes the time-reversal symmetry breaking detected by polar Kerr effect⁵³, the broken chiral symmetry at sample edges seen by STM-STs spectroscopies⁵⁴, the gap structure with point nodes through various bulk thermodynamic measurements^{55,56}. They point to an unconventional pairing state realized in UTe_2 . Some of those data are under discussion⁵⁷⁻⁵⁹ to finally pin down the precise pairing symmetry.

The main purposes of the present paper are three-fold, the first is to coherently explain these experimental facts with minimum assumptions: the off-axis high field phases³⁷⁻⁴⁰ with record high H_{c2} , in particular, the newly found phase diagrams²⁹ with the fields tilted from the bc -plane toward the a -axis, which was not covered before²⁸. The second is to revisit the phase diagram for $H \parallel b$ -axis containing newly discovered intermediate phase around TCP at 15T with the horizontal fourth transition line²¹ in order to sharpen our understanding. The third is to explain the Knight shift experiment performed on the second generation high-quality samples with $T_c=2.1\text{K}$, which shows the unusual drop for $H \parallel a$ -axis³⁰. These should be understood consistently and coherently. This task was not done in our series of papers on this material²⁴⁻²⁸.

The arrangement of the present paper is as follows: In the next section II, we outline our theoretical framework to analyze the experimental data mentioned. Then, we revisit the H - T phase diagram for $H \parallel b$ -axis, emphasizing the horizontal fourth transition line toward TCP in Sec III. In Sec IV we reproduce the off-axis phase diagrams, focusing on why the extremely high field H_{c2} is possible and why it is narrowly confined. In the following Sec V, we investigate the unusual Knight shift problems observed in detail, which is one of the main highlights of the present paper. We devote to the discussion in Sec VI and give a conclusion and summary in the final section.

The main difference from our series of papers²⁴⁻²⁸ lies in the fact that we further advance our theory, keeping the same theoretical framework. The formulation is the same as before, however, we repeat it for completeness as a full paper which is self-contained. In particular, we are now able to explain the newly found remarkable experimental facts: the horizontal fourth internal transition line, the off-axis phase diagrams, and the abnormally large Knight shift change for $H \parallel a$ -axis simultaneously and coherently. These new experiments become possible only by using newly synthesized high-quality samples with $T_c=2.1\text{K}$ ²².

II. GINZBURG-LANDAU THEORY FOR THREE COMPONENTS

A. Assumptions

We start with the most general Ginzburg-Landau (GL) theory for a spin triplet state^{24–28} to analyze the experimental data on UTe₂. We place three basic assumptions in the present paper:

(1) We assume a nonunitary A-phase-like pairing state described by the complex \mathbf{d} -vector $\mathbf{d}(k) = \phi(k)\boldsymbol{\eta} = \phi(k)(\boldsymbol{\eta}' + i\boldsymbol{\eta}'')$ with $\boldsymbol{\eta}'$ and $\boldsymbol{\eta}''$ being real vectors. $\phi(k)$ is the orbital part of the pairing function.

(2) The pairing function is classified under the overall symmetry $SO(3)^{\text{spin}} \times D_{2h}^{\text{orbital}} \times U(1)^{\text{gauge}}$ with the spin, orbital, and gauge symmetry, respectively^{60,61}, assuming the weak spin-orbit coupling scheme^{62,63}. The justification for this weak spin-orbit coupling (SOC) scheme lies in the experimental fact that the \mathbf{d} -vector rotation begins from the low fields, ~ 1 T for the c -axis³³, and ~ 5 T and its gradual rotation is completed at 15T for the b -axis³². This indicates that the spin-orbit coupling, which locks the \mathbf{d} -vector to crystalline lattices, is weak. We note that in the strong SOC scheme the gradual \mathbf{d} -vector rotation is not possible because the \mathbf{d} -vector locking energy is infinitely strong. The \mathbf{d} -vector may suddenly change when the two phases transform by a second-order or first-order phase transition because the spin symmetry is reduced to the crystalline symmetry D_{2h} , yielding four one-dimensional irreducible representations^{60,61}. These representations have distinct and non-degenerate transition temperatures except for the accidental degeneracy.

(3) To stabilize the nonunitary triplet pairing state⁶⁴, we assume the ferromagnetic fluctuations^{1,65–69} slower than the Cooper pair formation time. This allows us to introduce non-vanishing root-mean-square average $\sqrt{\langle M_a^2 \rangle}$ along the magnetic easy a -axis. This effective symmetry breaker makes the nonunitary state stable, otherwise unitary states obviously win over the nonunitary state. We do not need the static and/or spontaneous ferromagnetic transition, which is absent in UTe₂ even in the samples with $T_c=2.1\text{K}$ ⁵⁷. According to the recent NMR experiment on high-quality samples, Tokunaga et al⁶⁹ discover extremely slow longitudinal magnetic fluctuations on their T_2 measurements in the normal state although they do not specify whether or not ferromagnetic or antiferromagnetic.

We note that this postulation is supported by several previous examples similar to this situation: In UPt₃ the antiferromagnetic order at $T_N=7\text{K}$ lifts the degeneracy in the two-dimensional E_{1u} representation, but this antiferromagnetism is not a static and long-ranged order as checked by a variety of thermodynamic measurements, but only observed by the elastic neutron scattering⁷⁰, meaning that the antiferromagnetic fluctuations are fast enough thermodynamically and slow enough for neutron measurements. Yet they work as a symmetry breaker to split the SC transition temperature into two^{6–10}. An-

other example comes from the electron-doped cuprates where the antiferromagnetic fluctuations are reported to yield the band folding brought by a magnetic wave vector observed by photoemission experiments⁷¹

The $SO(3)^{\text{spin}}$ triple spin symmetry for the Cooper pair spin space allows us to introduce a complex three-component vectorial order parameter $\boldsymbol{\eta} = (\eta_a, \eta_b, \eta_c)$. The spin space symmetry is weakly perturbed by the $5f$ localized moments of the U atoms through the “effective” spin-orbit coupling felt by the Cooper pairs in the many-body sense. Our framework based on the weak SOC is sufficiently flexible to include the strong SOC as a limit^{72–74}. As detailed in the following, the three components of the order parameter originally had the same transition temperatures under the spin rotational symmetry, which is broken by either the applied field or the influence of the underlying magnetic subsystem.

B. GL free energy functional

Under D_{2h}^{orbital} symmetry, the GL free energy functional up to the quadratic order of $\boldsymbol{\eta}$ is expressed by

$$F = F_{\text{bulk}}^{(2)} + F_{\text{grad}} \quad (1)$$

where the free energy F consists with the bulk part $F_{\text{bulk}}^{(2)}$ and the gradient term F_{grad} . Each is given by

$$F_{\text{bulk}}^{(2)} = a_0(T - T_{c0})\boldsymbol{\eta} \cdot \boldsymbol{\eta}^* + b|\mathbf{M} \cdot \boldsymbol{\eta}|^2 + i\kappa\mathbf{M} \cdot \boldsymbol{\eta} \times \boldsymbol{\eta}^* \quad (2)$$

and

$$F_{\text{grad}} = \sum_{\nu=a,b,c} \{K_a|D_x\eta_\nu|^2 + K_b|D_y\eta_\nu|^2 + K_c|D_z\eta_\nu|^2\} \quad (3)$$

where b in Eq. (2) is a positive constant. The last invariant in Eq. (2) is essential for the following analyses and results from the nonunitarity of the pairing function in the presence of the moment \mathbf{M} , which breaks the $SO(3)^{\text{spin}}$ spin symmetry. K_a , K_b , and K_c in Eq. (3) are the effective masses along the a , b , and c -axes, respectively under an applied field with the vector potential \mathbf{A} . $D_i = -i\nabla_i + \frac{2\pi}{\Phi_0}A_i$ is the gauge invariant derivative, with Φ_0 being the quantum flux and A_i the vector potential component for the i -direction ($i = a, b, c$).

The magnetic coupling κ , which is a key parameter for characterizing UTe₂, is originally estimated⁷⁵ as

$$\kappa = T_c \frac{N'(0)}{N(0)} \ln(1.14\Omega_c/T_c), \quad (4)$$

where $N'(0)$ is the energy derivative of the normal density of states (DOS) $N(0)$, and Ω_c is the energy cut-off. This term results from the electron-hole asymmetry near the

Fermi level. κ indicates the degree of this asymmetry. This may be significant for a narrow band or the Kondo coherent band in the heavy Fermion material UTe₂. We can estimate $N'(0)/N(0) \sim 1/E_F$ with the Fermi energy E_F . Because $T_c=2$ mK and $E_F=1$ K in ³He, $\kappa \sim 10^{-3}$, while for UTe₂ $T_c \sim 1$ K and $E_F \sim T_K$ with the Kondo temperature $T_K \sim 30$ K³, $\kappa \sim 10^{-1}$. We also note that the sign of κ can be either positive or negative, depending on the detailed energy dependence of DOS at the Fermi level because it is $\propto N'(0)$. If $\kappa > 0$ ($\kappa < 0$), the $\uparrow\uparrow$ ($\downarrow\downarrow$) pair appears at higher T . Thus, the KS remains unchanged (decreases) below T_c . We will find later that $\kappa < 0$ in UTe₂. That is, we now determine the sign of κ

We introduce $\eta_{\pm} = (\eta_b \pm i\eta_c)/\sqrt{2}$ for $\mathbf{M} = (M_a, 0, 0)$ where we define the a -axis as the magnetic easy axis. η_+ (η_-) corresponds to the spin $\uparrow\uparrow$ ($\downarrow\downarrow$) pair or the A₁(A₂) phase. The spin quantization axis is defined relative to the \mathbf{M} direction, i.e., the magnetic easy a -axis. Because of the magnetic coupling term $i\kappa\mathbf{M} \cdot \boldsymbol{\eta} \times \boldsymbol{\eta}^*$, the spin direction for the Cooper pair may change. Here it is convenient to introduce the Cooper pair spin moment direction \mathbf{S} as

$$\mathbf{S} = i \frac{\boldsymbol{\eta} \times \boldsymbol{\eta}^*}{|\boldsymbol{\eta}|^2}. \quad (5)$$

We notice the case: when the direction \mathbf{S} is fixed, the magnetization \mathbf{M} direction is chosen to lower the magnetic coupling energy $i\kappa\mathbf{M} \cdot \boldsymbol{\eta} \times \boldsymbol{\eta}^*$. From Eq. (2) the quadratic term $F_{\text{bulk}}^{(2)}$ becomes

$$F_{\text{bulk}}^{(2)} = a_0 \{ (T - T_{c1})|\eta_+|^2 + (T - T_{c2})|\eta_-|^2 + (T - T_{c3})|\eta_a|^2 \} \quad (6)$$

with

$$\begin{aligned} T_{c1,2}(M_a) &= T_{c0} \pm \frac{\kappa}{a_0} M_a, \\ T_{c3}(M_a) &= T_{c0} - \frac{b}{a_0} M_a^2. \end{aligned} \quad (7)$$

Although the actual second transition temperatures are modified by the fourth order GL terms²⁴⁻²⁶, we ignore this correction and maintain the expressions for the transition temperatures for clarity.

The root-mean-square average $\sqrt{\langle M_a^2 \rangle}$ of the FM fluctuations along the magnetic easy a -axis was simply denoted by M_a , shifting the transition temperature T_{c0} and split it into T_{c1} , T_{c2} , and T_{c3} given above. According to this, T_{c1} (T_{c2}) increases (decreases) linearly as a function of M_a , whereas T_{c3} decreases quadratically as M_a^2 from the degeneracy point $M_a = 0$. The three transition lines meet at $M_a=0$, where the three components η_i ($i = +, -, a$) are all degenerate. Thus, away from the degenerate point at $M_a=0$, the A₀ phase beginning at

T_{c3} quickly disappears from the phase diagram in general. Below T_{c2} , the two components η_+ and η_- coexist, symbolically denoted by A₁+A₂. Note that, because their transition temperatures are different, A₁+A₂ is not the so-called A-phase, which is unitary, but here is generically nonunitary except at the degenerate point $M_a=0$ where the totally symmetric phase is achieved with the time reversal symmetry preserved. This occurs under pressure at the critical pressure $P_{\text{cr}}=0.15$ GPa for $T_c=2.1$ K samples when $T_{c1}=T_{c2}$. The A₁+A₂ phase is the so-called distorted A phase¹⁷. Similarly, below T_{c3} , all the components coexist; A₁+A₂+A₀ is realized. The naming such as A₁, A₂, and A₀ is retained even when the spin quantization axis changes according to the d-vector rotation under fields. Thus A₁ and A₂ are meant to distinguish between the spin $\uparrow\uparrow$ pair and spin $\downarrow\downarrow$ pair with respect to the spin quantization axis. Hereinafter, we redefine the notation $\kappa/a_0 \rightarrow \kappa$.

C. Upper critical field

To construct the phase diagrams for various field orientations, we need to derive the H_{c2} expression. This can be done by starting with the free energy functional in Eq. (1) where Eq. (2) is rewritten as in Eq. (6). The form of Eq. (3) shows that the H_{c2} for the three components each starting at T_{c_j} ($j = 1, 2, 3$) given by Eq.(7) intersect each other, never avoiding or leading to a level repulsion. The level repulsion may occur for the pairing states belonging to multi-dimensional representations (see for example [76–79] in UPT₃). Thus, each component is independent within the quadratic terms. The total GL free energy density F , consisting with Eqs. (3) and (6) under the external magnetic field H in terms of the superconducting order parameter η_{\pm} is given by

$$F = \sum_{i=\pm} \{ a_0(T - T_{c,i})|\eta_i|^2 + K_a|D_x\eta_i|^2 + K_b|D_y\eta_i|^2 + K_c|D_z\eta_i|^2 \}. \quad (8)$$

The variation with respect of η_i^* results in

$$a_0(T - T_c)\eta_i + (K_a D_x^2 + K_b D_y^2 + K_c D_z^2)\eta_i = 0. \quad (9)$$

The upper critical field H_{c2} is given as the lowest eigenvalue of the linearized GL equation or Schrödinger type equation of a harmonic oscillator⁸⁰ as,

$$H_{c2,j}^{(\pm)}(T) = \alpha_0^j(T_{c0} \pm \kappa M_a - T) \quad (10)$$

with $j=a, b$, and c -axis. We have introduced, $\alpha_a^0 = \frac{\Phi_0}{2\pi\sqrt{K_b K_c}} a_0$, $\alpha_b^0 = \frac{\Phi_0}{2\pi\sqrt{K_c K_a}} a_0$, and $\alpha_c^0 = \frac{\Phi_0}{2\pi\sqrt{K_a K_b}} a_0$. These coefficients determine the initial slopes of the upper critical fields. $H_{c2,j}^{(+)}$ and $H_{c2,j}^{(-)}$ are the upper critical fields for $\uparrow\uparrow$ and $\downarrow\downarrow$ pairs, or the A₁ and A₂ phases.

Expressing Eq. (10) in a form by suppressing the index j , we obtain in a general form:

$$H_{c2} - \alpha_0 \kappa M(H_{c2}) = \alpha_0 (T_{c0} - T). \quad (11)$$

The right-hand side of Eq. (11) is now

$$H_{c2}^{\text{orb}}(T) = \alpha_0 (T_{c0} - T) \quad (12)$$

for an unperturbed upper critical field owing to the orbital depairing limit with T_{c0} whose maximum value is given by $H_{c2}^{\text{orb}}(T=0) = \alpha_0 T_{c0}$. On the left-hand side of Eq.(11) we define the effective field H_{eff} by

$$H_{\text{eff}} = H_{\text{ext}} - \alpha_0 \kappa M(H_{\text{ext}}). \quad (13)$$

This implies that the external field H_{ext} is reduced by $\alpha_0 \kappa M(H_{\text{ext}})$, a situation similar to that in CeRh_2As_2 ²⁷ and also somewhat to the Jaccarino and Peter mechanism⁸¹ in a spin-singlet superconductor. The upper bound of the orbital depairing field of $H_{c2}^{\text{orb}}(T)$ for the a -axis, for example, is determined by

$$H_{c2}^{\text{orb}}(T \rightarrow 0) = \alpha_0^a T_{c0} = \frac{\Phi_0}{2\pi\sqrt{K_b K_c}} a_0 T_{c0}. \quad (14)$$

This is given by the expression in the clean limit: $H_{c2}^{\text{orb}}(T) = \Phi_0/2\pi\xi^2$, where the coherence length $\xi = \hbar v_F/\pi T_{c0}$. At $H_{c2}^{\text{orb}}(T=0)$, the inter-vortex distance becomes comparable to the core size ξ . From now on, we suppress the subscript ext; thus, $H_{\text{ext}} \rightarrow H$.

At $T=0$, the absolute value of H_{eff} is bounded by

$$|H_{c2} - \alpha_0 \kappa M(H_{c2})| \leq H_{c2}^{\text{orb}}(T=0) = \alpha_0 T_{c0} \quad (15)$$

for $H_{c2}(0)$ to be a solution of Eq. (11). The right-hand side is determined by the material parameters in terms of the Fermi velocity v_F through the coherent length ξ and the transition temperature T_{c0} . Thus, the absolute upper limit (AUL) $H_{c2}^{\text{AUL}}(0)$ can be enhanced at $T \rightarrow 0$ over $H_{c2}^{\text{orb}}(T=0)$, namely,

$$H_{c2}^{\text{AUL}}(T) \geq H_{c2}^{\text{orb}}(T). \quad (16)$$

$H_{c2}^{\text{AUL}}(T)$ is a clue to understand the extremely high upper critical field in UTe_2 as seen shortly.

III. PHASE DIAGRAM FOR $H \parallel b$ -AXIS WITH TETRA-CRITICAL POINT

A. Construction of the phase diagram

We start to investigate the phase diagram for $H \parallel b$ -axis, which has the richest structure with a tetra-critical

point among three principal directions. To understand it, let us first examine the magnetization curve $M(H \parallel b) = M_b(H)$ measured by Miyake et al⁸². As shown in the lower panel of Fig. 1 by the red line, $M_b(H)$ exhibits a meta-magnetic first-order phase transition at $H_m = 34\text{T}$ with the large magnetization jump $\sim 0.5\mu_B/\text{U-atom}$. Correspondingly, as defined in Eq. (13) the effective magnetic field H_{eff} exerted to the conduction electrons, which is denoted by the green curve is reduced strongly compared with the external field H_{ext} shown there. We have fixed the parameter values as follows: $\alpha_0 = 27\text{T/K}$ taken from the experimental data determined by 2.1K samples⁸³. $\kappa = 2.7\text{K}/\mu_B$. This yields $T_{c1}=2.1\text{K}$, $T_{c0}=1.25\text{K}$, and $T_{c2}=0.44\text{K}$ under the assumption $M_a = 0.3\mu_B/\text{U-atom}$.

For the A_1 phase with the transition temperature $T_{c1}=2.1\text{K}$, the allowed region for their $H_{c2}^{\text{orb}}(A_1) = \alpha_0 T_{c1}$ in Eq. (14) denoted by the light gray band is exceeded at $\sim 22\text{T}$. Thus the A_1 phase ceases to exist beyond this field at $T=0$.

On the other hand, the A_2 phase with $T_{c2}=0.4\text{K}$ which has a narrower allowed region (dark gray band) defined by $H_{c2}^{\text{orb}}(A_2) = \alpha_0 T_{c2}$ compared with that for the A_1 phase by a factor $T_{c2}/T_{c1}=0.2$. Thus this A_2 phase terminates at a lower field around 7T. However, once the d-vector rotation occurs at $H_{\text{rot}}=15\text{T}$ so that the Cooper pair spin \mathbf{S} becomes parallel to the b -axis to reduce the Zeeman energy, then it appears again and grows with $T_{c2} = T_{c0} + \kappa M_b(H)$. Note the switching $-M_a(H)$ to $+M_b(H)$ in Eq. (7) upon the d-vector rotation. As displayed in the upper panel of Fig. 1, the intersection point at $H_{\text{tetra}}=15\text{T}$ where the four second order phase transition lines meet to form a tetra-critical point (TCP). The rising $T_{c2}(M_b)$ line terminates at the meeting point with the curve starting at H_{c2}^{AUL} . This defines the absolute upper limit of $H_{c2}^{\text{orb}}(A_2)$ for the A_2 phase beyond which the green curve is outside the allowed region colored by the dark gray.

Note that $H_{c2}^{\text{AUL}}(T)$ for $H_m < H_{c2}^{\text{AUL}}(T) < H_{c2}^{\text{AUL}}(T=0)$ does not exist because the green curve is outside the allowed region indicated by the dark gray above H_m . Therefore, it exists only in the field region between the intersection point and the point below H_m . We also notice that the green line H_{eff} returns eventually to the allowed region in higher fields denoted by H_{c2}^{AUL} (upper) and H_{c2}^{AUL} (lower), but in this field the DOS available for superconductivity is below the normal DOS, thus is not eligible for the A_2 phase to reappear as explained shortly.

B. Tetra-critical point with horizontal fourth line

As seen from Fig. 2(c), along H_{c2} starting at $T_{c1}=2\text{K}$, the A_1 phase characterized by $\boldsymbol{\eta}_b + i\boldsymbol{\eta}_c$ becomes non-vanishing. At the tetra-critical point (TCP), $\boldsymbol{\eta}_a + i\boldsymbol{\eta}_c$ emerges associated with T_{c2} . Thus along the H_{c2} line just at TCP where $\boldsymbol{\eta}_a=0$, the d-vector can complete the rotation from $\boldsymbol{\eta}_a + i\boldsymbol{\eta}_c$ to $\boldsymbol{\eta}_b + i\boldsymbol{\eta}_c$. Simultaneously, above

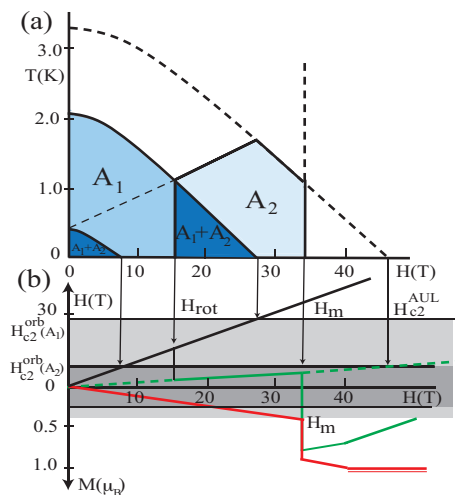


FIG. 1: Upper panel (a): Constructed phase diagram for $H \parallel b$ -axis in the T vs H plane. The A_1 , the mixture A_1+A_2 , and A_2 correspond to LSC, MSC, and HSC respectively along the H axis. Note that the A_2 exists in the lowest H and lowest T around the origin. The dotted lines are not realized. Lower panel (b): $H_{\text{eff}}(H)$ is indicated by the green curve, which is derived from the observed magnetization curve $M_b(H)$ denoted by the red line. H_{rot} is the field where the d-vector rotation completes, starting around 5T. The two horizontal bands colored by light and dark gray indicate the allowed field regions $H_{c2}^{\text{orb}}(A_1)$ and $H_{c2}^{\text{orb}}(A_2)$ for the A_1 and A_2 phases respectively. The dotted green line is not realized. The green line reenters the allowed region at $H_{c2}^{\text{AUL}}(\text{lower})=58\text{T}$ and exits at $H_{c2}^{\text{AUL}}(\text{upper})=73\text{T}$ in the higher field (see Fig. 5).

this particular field $H_{\text{TCP}}=15\text{T}$ in $T=0$, this A_2 phase enters the allowed region denoted by the dark gray as seen from the green line of the lower panel of Fig. 1. Thus the fourth internal transition line toward TCP is always horizontal in the H - T phase diagram. It is true for the phase diagrams for $H \parallel b$ -axis under pressure (see Figs. 19(b1), (b2), and (b3)).

Here it is important to notice that if the crossing of the second order phase transition lines is due to the degeneracy of the orbital part of the pairing function η_i with i being the orbital index, there always exists the so-called gradient coupling term $(D_i \eta_j)^*(D_j \eta_i)$ with D_i the gauge invariant derivative in the GL functional^{76–79}. This invariant inevitably leads to “the level repulsion” so that the four transition lines are always anti-crossing. This means that since the experimental data exhibit no anti-crossing, the degeneracy comes from the spin part of the pairing function. We emphasize that this experimental observation of the tetra-critical point is crucial in choosing the proper pairing function.

Therefore, as shown in Fig. 2 (b) the A_1 phase is simply overlapped by the A_2 phase in Fig. 2 (a) to complete the overall phase diagram shown in Fig. 2 (c). This means physically that the two A_1 and A_2 phases interact weakly, allowing us to treat it in the weak coupling GL framework

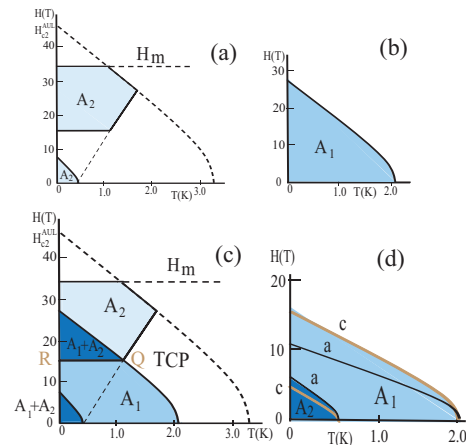


FIG. 2: (a) and (b) indicate the H - T phase diagrams for the A_1 and A_2 phases separately. From (a), it is understood that the A_2 phase is reentrant. The isolated high field part conforms to HSC. (c) shows the combined total phase diagram for $H \parallel b$ -axis in the H - T plane. The tetra-critical point (TCP) at $H_{\text{TCP}}=15\text{T}$ consists of the horizontal fourth line above which the A_2 phase reappears, the positive sloped H_{c2} belongs to A_2 , and the negative sloped internal line comes from A_1 . The dotted lines are not realized, displayed for guidance. The expected straight dotted line starting at $T_{c2}=0.4\text{K}$ is not realized. (d) shows the phase diagrams for $H \parallel a$ -axis and $H \parallel c$ -axis, containing the small pocket region for the A_2 phase.

as we apply. The fourth order term of the interaction between them in our GL functional can be neglected. The overlapping part between $H=15\text{T}$ and 27T denoted by the darker color in Fig 2(c) consists of the mixture of the A_1 phase and A_2 phases.

C. Horizontal fourth line

According to the experimental data by Sakai, et al²¹, the fourth phase transition line toward TCP is almost horizontal. Here we elaborate its reasons why it is so:

- (1) We first notice that this transition line comes from the order parameter $\Delta_{b\downarrow}$ with the down spin of the Cooper pair whose quantization axis $\parallel b$ -axis. This state only senses the M_b component, which is a fundamental assumption throughout the present paper, even during the d-vector rotation process.
- (2) Thus the green curve for $M_b(H)$ in Fig. 2 is relevant after the d-vector rotation is completed.
- (3) The equi- M_b lines are all horizontal at the lower temperature region in Fig. 2(c), meaning that Fig. 1(b) is basically applicable for finite temperatures.
- (4) The position R in Fig. 2(c) at $T=0$ for H_{rot} with $M_b = M_b(H_{\text{rot}})$ must connect to the point Q with the same M_b which is on the T_{c2} line with $T_{c2} = T_{c0} + \kappa M_b(H_{\text{rot}})$.
- (5) Namely, Q satisfies the condition for the phase boundary. By increasing H under the fixed T , Q becomes the

onset for the A_2 phase.

(6) Moreover the Q point is precisely the point which allows the completion of the d-vector rotation because the three components of the order parameter are all degenerate there.

In Appendix A, we examine the phase diagram for the $T_c=1.6\text{K}$ samples.

IV. OFF-AXIS HIGH FIELD PHASES

When the field is tilted from the b -axis by a few degrees either toward the a -axis or the c -axis, the above phase diagram in Figs. 1 and 2(c) is smoothly modified. This is because the projection of $M_b(H)$ onto the external field is reduced, thus correspondingly H_{eff} becomes smaller, resulting in $H_{c2}^{\text{AUL}} < H_m$. The whole part of the A_2 phase appears below H_m while a part of the A_2 phase is masked by H_m for $H \parallel b$ -axis in Fig 2.

A. H - T phase diagram in $b \rightarrow c$

When the field is tilted by the larger angles θ measured from the b -axis toward the c -axis, the high field phase, or HSC appears above H_m for a certain angle region. The forgoing arguments for $H \parallel b$ -axis are extended to this case by changing

- (1) the magnetization curve $M_b(H)$ taking the projection onto the applied field (see Fig. 8(b) in Ref. 26).
- (2) the allowed region $\pm\alpha_0(\theta)T_{c2}$ where

$$\alpha_0(\theta) = \alpha_0^b \cos \theta + \alpha_0^c (1 - \cos \theta) \quad (17)$$

with α_0^b (α_0^c) the value for the b (c)-axis by taking into account the observed H_{c2} anisotropy for the LSC phase due to the Fermi velocity change. α_0^b is estimated by the initial slope of H_{c2} at $T_c=2.1\text{K}$ as $\alpha_0^b = -dH_{c2}/dT = -27\text{T/K}$ ($\alpha_0^c = -6\text{T/K}$), which is known experimentally⁸³. We assume the angle dependence of $\alpha(\theta)$ to be true for the high field A_2 phase too because the Fermi velocity is the same for both phases. Formally, $H_{c2}^{\text{AUL}}(\theta)$ is given by

$$H_{c2}^{\text{AUL}}(\theta) = \frac{\alpha_0(\theta)T_{c0}}{1 - \alpha_0(\theta)\kappa\chi_b \cos \theta} \quad (18)$$

where χ_b is the susceptibility along the b -axis. This means that the extra-enhancement of $H_{c2}^{\text{AUL}}(\theta)$ may come from this renormalization in the denominator. However in the following we maintain to use the simplest formula without the renormalization for our analysis.

- (3) the d-vector rotation field is assumed to vary as

$$H_{\text{rot}}(\theta) = \frac{H_{\text{rot}}(\theta = 0)}{\cos \theta}, \quad (19)$$

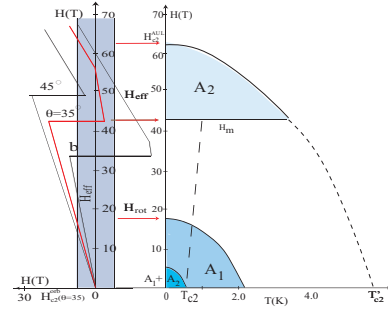


FIG. 3: The constructed phase diagram in the H - T plane for $\theta = 35^\circ$. The left side panel: The allowed region denoted by the gray band with $\pm H^{\text{orb}}(\theta = 35^\circ) = 18\text{T}$. $H_{\text{eff}}(\theta = 35^\circ)$ is shown by the red line together with those with $\theta = 0^\circ$ ($\parallel b$) and 40° for reference. Above H_m , it enters the allowed region up to H_{c2}^{AUL} , stabilizing the A_2 phase as shown in the right panel where the whole H - T phase diagram is displayed including the A_1 phase. $H_{\text{rot}}(\theta = 35^\circ) = 16\text{T}/\cos 35^\circ = 19.5\text{T}$ just fails to yield the tetra-critical point. There is no MSC at this angle.

reflecting the fact that the projection of M_b onto the external field matters since the coupling energy is proportional to $\kappa \mathbf{M}_b(H) \cdot \boldsymbol{\eta} \times \boldsymbol{\eta}^*$. This idea is the same as $H_m(\theta) = H_m(\theta = 0)/\cos(\theta)$ for the metamagnetic transition, which is known to hold experimentally³.

We display an example of this procedure for $\theta = 35^\circ$ in Fig. 3 where the panel on the left hand side shows the effective field H_{eff} as a function of the external field H by the red curve relative to the allowed region and the resulting phase diagram is in the right panel. Since the red curve for the A_2 phase comes back in the allowed region above H_m and stays up to H_{c2}^{AUL} , the A_2 phase reentrants above H_m while in the lower field, it disappears. Here the meta-magnetic transition is important for the A_2 phase to reappear because H_{eff} is greatly reduced there. Also the extra DOS $\gamma(H) (> \gamma_N)$ becomes available just above H_m as explained later.

We note here that the combination between $H_{c2}^{\text{AUL}}(\theta)$ and the realized field region for $\gamma(H) > \gamma_N$ determines the high field A_2 phase. As shown in Fig. 4 for $H \parallel (011)$ -direction ($\theta \sim 23.8^\circ$) the phase diagram is most intricate where the MSC phase and HSC phase coexist. As seen from Fig. 4, $H_{\text{eff}}(H)$ denoted by the red line is within the allowed region in between $H_{\text{rot}} < H_{\text{eff}} < H_{c2}^{\text{AUL}} \sim 30\text{T}$ below H_m . Then it reappears above H_m up to the field for the extra DOS to be available. Note that H_{c2}^{AUL} (upper) is far above, but it is not realized.

To understand how $H_{c2}(\theta)$ becomes maximal around $\theta \sim 40^\circ$, we summarize various lines which constrain the realized H_{c2} in Fig. 5. As seen from it, LSC containing the $A_1 + A_2$ phase at the bottom occupies the lowest field region and varies as a function of θ according to the Fermi velocity or mass anisotropy. MSC appears in the middle fields above H_{rot} , which forms the tetra-critical point in the H - T phase diagram for a given θ . This is followed

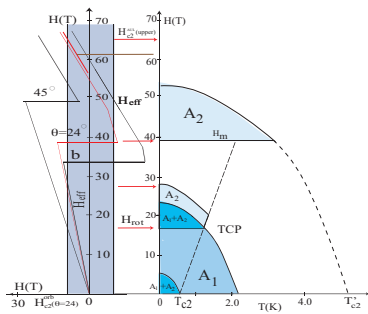


FIG. 4: Phase diagram for $\theta = 24^\circ$. The left side panel: The allowed region denoted by the vertical gray band with $\pm H_{c2}^{\text{orb}}(\theta = 24^\circ)$. $H_{\text{eff}}(\theta = 24^\circ)$ is shown by the red line together with those with $H \parallel b$ and $\theta = 45^\circ$. Above H_m it enters the allowed region up to $H_{c2}^{\text{AUL}}(\text{upper})$. The upper bound of the A_2 phase as shown in the right hand panel is limited by the region $\gamma > \gamma_N$. In the middle fields, the A_2 phase reappears above H_{rot} . We note that $H_{\text{rot}}(\theta = 24^\circ) = 16\text{T}/\cos 24^\circ = 17.5\text{T}$ yields the tetra-critical point at that field.

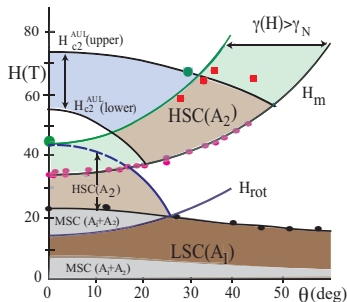


FIG. 5: The phase diagram in the H - θ plane. The gray band is defined by the upper and lower H_{c2}^{AUL} . The green band is defined by the region for $\gamma(H) > \gamma_N$. In the overlapping region of the two bands HSC(A_2) phase appears, yielding the highest H_{c2} around $\theta = 35^\circ$. In the low angle θ region HSC(A_2) phase appears below H_m below which MSC(A_2+A_2) exists. Inside MSC(A_1) in lower field bottom region MSC(A_2+A_2) appears. H_m and H_{rot} behave like $\propto 1/\cos(\theta)$. The red squares are the superconducting transitions³⁷. The round green dots in $\theta = 0^\circ$ and 28° are the upper limit of the observed points^{82,84} at which $\gamma(H) = \gamma_N$.

by HSC(A_2) appearing just above H_{rot} and below H_m . As $H_{\text{rot}}(\theta)$ becomes higher as θ increases and eventually leaves the LSC region and also H_{c2}^{AUL} sharply decreases, MSC and HSC cease to exist below H_m . This happens at around $\theta \sim 30^\circ$. Near this angle, the higher HSC(A_2) appears above H_m , whose region is sandwiched by the band defined by $H_{c2}^{\text{AUL}}(\text{upper})$ and by $H_{c2}^{\text{AUL}}(\text{lower})$, and the other band defined by the region $\gamma(H) > \gamma_N$. The overlapping field region of the two bands above H_m denoted by HSC(A_2) in Fig. 5 gives rise to the highest upper critical field. It is understood that the coexisting two HSCs below and above H_m are rather special and

only appear in the limited $\theta \sim 24^\circ$. Generically the H - T phase diagram belong to either that in $H \parallel b$ -axis shown in Fig. 2(c) or that shown in Fig. 3.

In connection with the phase diagrams above, we study comparatively the cases in URhGe in Appendix B, and discuss the phase diagrams consisting with multiple phases under pressure to strengthen our idea in Appendix C.

B. High field phases in $bc \rightarrow a$

It is interesting to examine how the high field phase HSC(A_2) of the bc -plane displayed in Fig. 5 evolves when the field direction is tilted from this plane toward the a -axis because our theory can be checked further. This is experimentally done by Lewin et al²⁹. They show further higher H_{c2} surpassing 70T or more limited still experimentally. In the following we keep the same set of the parameters and the procedures used so far. To construct the phase diagrams for H tilted from the bc -plane toward the a -axis by the angle ϕ , we need to know magnetization curves for $M_b(H)$ for arbitrary angle ϕ first.

The magnetization component $M_b(H)$ projected onto the field direction is obtained by considering the fact that all the meta-magnetic transition fields H_m are scaled and collapsed into a single curve independent of the angle θ , or all the $H_m(\phi)$ curves for various θ are scaled to lead to the identical curve. This remarkable independence termed as ‘‘orthogonality’’ by Lewin et al²⁹ allows us to reproduce $M_b(H)$ for arbitrary angle ϕ . Namely starting with the known magnetization curve $M_b(H)$ for $H \parallel b$ -axis, the $M_b(H)$ component and the jump of $M_b(H)$ for the angle ϕ are obtained by shifting $H_m(\phi)$ and by taking the projection onto the field direction. The resulting $M_b(H)$ components for various ϕ values in $\theta = 40^\circ$, for example, are shown by the red curves in Fig. 6. These lead to the effective fields H_{eff} displayed by the blue curves for the corresponding ϕ values. Thus the curves are within the allowed region for HSC to exist, indicated by the double sided arrows there.

According to Fig. 6, we draw the phase diagram for $\phi=40^\circ$ in the top panel in right hand side in Fig. 7. It is seen from Fig. 7 that above $H_m(\phi)$ the HSC region appears from $\phi=0$ up to $\phi \sim 10$ and quickly disappear as ϕ increases, which is compared with the experimental data shown in the bottom panels by Lewin et al²⁹. Similarly, we can evaluate the case for $\theta = 8^\circ$ by the same way mentioned whose result is shown in the left column of Fig. 7. It is seen that starting with $\phi=0$ where the HSC is absent, by increasing the angle ϕ the HSC gradually appears and fades away. In the corresponding experimental phase diagram shown in the bottom panel is seen barely the tiny HSC regions in high ϕ angles. The evolution of the HSC in the bc -plane toward the a -axis is satisfactorily reproduced in a qualitative level. This is another demonstration of the correctness of our theory.

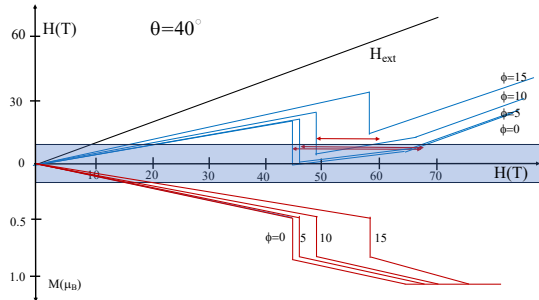


FIG. 6: Magnetization curves (red curves) of the $M_b(H)$ component projected onto the applied field direction for the selected angles ϕ measured from the bc -plane under the fixed angle $\theta = 40^\circ$. The corresponding blue curves indicate the effective fields relative to the external field H_{ext} . The allowed region is shown by the gray band along the $H(T)$ axis. The double sided red arrows show the HSC(A_2) allowed.

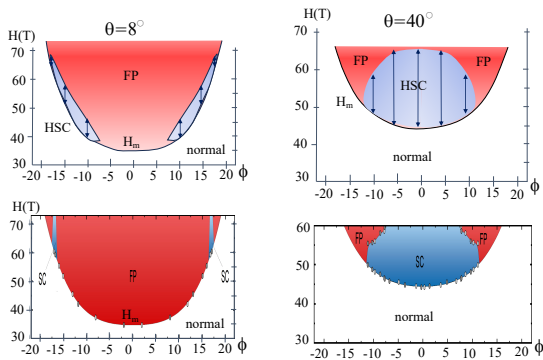


FIG. 7: The resultant HSC regions as a function of ϕ for the $\theta=8^\circ$ and 40° cases (upper panel). The experimental data for the two cases are referred to by Lewin et al²⁹ (lower panel). For the case of $\theta=40^\circ$ the HSC appears at $\phi=0$ above H_m while it is absent for $\theta=8^\circ$. This corresponds to these in Fig. 5.

These results can be easily understood physically and intuitively as follows: As shown in Fig. 8 where the contour map of $H_m(\theta, \phi)$ is displayed as the functions of θ and ϕ , together with the experimental data for the HSC to exist²⁹ in this plane. The equi- H_m contour forms as an elliptic curve obtained by combining the two data sets of the b -axis \rightarrow c -axis results⁸² and the bc -plane \rightarrow a -axis results²⁹. The region sandwiched by $H_m(\theta, \phi)=38\text{T}$ and 50T is for the HSC to exist. For example, along the $\phi=0$

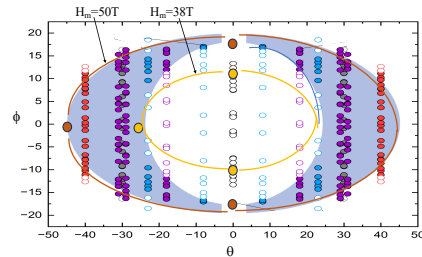


FIG. 8: The experimental data points in the θ - ϕ plane which correspond to the HSC to exist indicated by the filled circles²⁹. The grey regions indicate the HSC regions projected onto the θ - ϕ plane. Between the two contours of $H_m=38\text{T}$ and 50T there exist the HSC phases according to the present theory.

axis we have seen from Fig. 5 that the HSC exists from $H=38\text{T}$ up to $H\sim 50\text{T}$ occurring at $\theta \sim 45^\circ$ indicated by the HSC(A_2). This squared-like region of the HSC in Fig. 5 moves up to a higher field when H is tilted toward the a -axis. Thus in Fig. 8 the HSC corresponds to the grey regions in between the two contours as shown by the experimental data with the filled points. It is also understood from Fig. 5 that the maximum H_{c2} of UTe_2 under ambient pressure is less than or nearly equal to 70T throughout the (θ, ϕ) -plane. There exists no higher H_{c2} hidden in UTe_2 .

V. KNIGHT SHIFT

A. KS for $H \parallel a$ -axis

The Knight shift for $H \parallel a$ -axis decreases below T_c for high-quality samples, which is contrasted with that for $T_c=1.6\text{K}$ samples without KS decreasing³⁴. We now discuss this phenomenon in terms of our nonunitary scenario. At first sight, it is at odds with it because the Cooper pair polarization $\mathbf{S} \parallel a$ -axis at low H . We solve this puzzle in the following.

We first note that the absolute value of $|\Delta K_a|$ for the a -axis is abnormally large³⁰, namely $|\Delta K| = 3.7 \sim 4.2\chi_N$ as described in Appendix E. To understand the negative and large $|\Delta K_a|$ we examine the GL coupling term $\kappa \mathbf{M}_a \cdot \boldsymbol{\eta} \times \boldsymbol{\eta}^*$ between the magnetization along the a -axis and the d -vector. Under the quantization axis parallel to the a -axis, it can be written as

$$\kappa \mathbf{M}_a \cdot \boldsymbol{\eta} \times \boldsymbol{\eta}^* = \kappa M_a (\Delta_\uparrow^2 - \Delta_\downarrow^2). \quad (20)$$

Here we employ the notations Δ_\uparrow and Δ_\downarrow to explicitly express the spin moment direction. If $\kappa < 0$, which we consider in the following, then the split transition temperatures T_{c1} and T_{c2} are identified $T_{c1} = T_{c\downarrow}$ and $T_{c2} = T_{c\uparrow}$ respectively. Namely upon lowering T , Δ_\downarrow is condensed

first and further lowering T , Δ_\uparrow is followed at T_{c2} . Since the Cooper pair spin moment \mathbf{S} defined by Eq. (5) is locked by the magnetization direction \mathbf{M}_a through the above GL coupling, not the external field, independent of the positive or negative direction of the external field \mathbf{H} , Δ_\downarrow appears below T_{c1} because it is locked by \mathbf{M}_a . This situation is contrasted in the conventional case where Δ_\uparrow always appears first to save the Zeeman energy even if the external field direction is reversed, leading to the paramagnetic response $\chi_s = +\chi_N > 0$. Thus it immediately leads to $\Delta K_a < 0$ below T_{c1} . The A_1 phase with Δ_\downarrow responds diamagnetically to the external field.

Let us consider the magnitude of $|\Delta K_a|$. The spin susceptibility $\chi_a(T)$ near T_{c1} is calculated starting with the GL functional given by Eq. (6), following the procedure by Takagi⁸⁵ on the $^3\text{He-A}$ phase under applied fields,

$$f = a_0(T - T_{c1}(H))\Delta_\downarrow^2 \quad (21)$$

with $a_0 = N(0)/T_{c1}$ and $T_{c1} = T_{c0} + \frac{\kappa}{a_0}M_a$. The magnetization change δM is derived as

$$\delta M = -\frac{\partial f}{\partial H} = a_0\kappa\frac{\partial M}{\partial H}\Delta_\downarrow^2. \quad (22)$$

This leads to

$$\frac{\delta M}{M_{\text{Pauli}}} = \frac{\Delta_\downarrow^2}{2\mu_B H T_{c1}} \frac{\kappa}{a_0} \frac{\partial M}{\partial \mu_B H}. \quad (23)$$

Substituting the weak coupling BCS value for $\Delta_\downarrow = 1.75T_{c1}$, $\frac{\kappa}{a_0} = 2.7\text{K}/\mu_B$ and $\frac{\partial M}{\partial \mu_B H} = 0.07\mu_B/\text{K}$ at $H=1\text{T}$ ⁸², we obtain $\delta M/M_{\text{Pauli}} = 1.3$, which is smaller than the estimated observe value $3.7\sim 4.2$. If taking into account the strong coupling value $\Delta_\downarrow = (1.5 \sim 2.0) \times 1.75T_{c1}$, we find $\delta M/M_{\text{Pauli}} = 2.9 \sim 5.2$, agreeing with the experimental estimate. Note that the strong coupling effect is evident from the large specific heat jump⁸⁶ $\Delta C/\gamma_N T_{c1} \sim 2.7$ with the $T_c=2.1\text{K}$ samples compared with 1.43 in BCS. This agreement implies that the mechanism of the KS along the a -axis is quite different from the usual case for $\mathbf{H} \perp \mathbf{S}$. This mechanism is somewhat similar to that in $^3\text{He-A}_1$ ⁸⁵. In Appendix C we estimate the KS value different from this due to Miyake⁸⁷, which yields a similar value.

As shown in Fig. 9(a1), with decreasing T the T -dependence of $\Delta K(T)$ at low H exhibits a large drop below T_{c1} . Below T_{c2} , or $T_{c\uparrow}$ the decrease stops and slightly increases because Δ_\uparrow starts appearing as shown in Fig. 2(d). It is seen from Fig. 9(a2) that with increasing H , $\Delta K(H)$ at low T shows a decrease toward $H_{c2\uparrow}$ at which $\Delta_\uparrow = 0$ as shown in Fig. 2(d). Then it increases up to $H_{c2}^a=12\text{T}$ toward the normal state because in this field region Δ_\downarrow diminishes toward it.

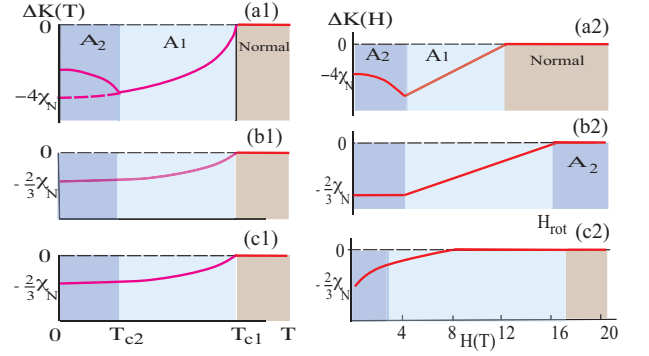


FIG. 9: The Knight shift ΔK or the spin susceptibilities in the superconducting state as functions of T (left column) at low H and H (right column) for three field orientations. Upon lowering T , $\Delta K(T)$ strongly decreases below T_{c1} for $H \parallel a$ and increases below T_{c2} when the A_2 appears (a1) while $\Delta K(T)$ behaves as in the Yosida function for b (b1) and c (c1) axes. $\Delta K(H \parallel a)$ decreases in the A_2 state and increase when entering the A_1 state with increasing H (a2). $\Delta K(H \parallel b)$ remains a constant at lower H and increases when entering the A_1 state with increasing H (b2). $\Delta K(H \parallel c)$ keeps gradually increasing and reaches $\Delta K=0$ around 8T (c2).

B. KS for $H \parallel b$ -axis

As shown in Fig. 9(b1), with decreasing T the T -dependence of $\Delta K(T)$ at low H for $H \parallel b$ -axis exhibits a drop below T_{c1} because \mathbf{S} points to the a -axis or one of the two d-vector components is parallel to the field direction. Thus $\Delta K(T \rightarrow 0) = -\frac{2}{3}\chi_N$. The overall T -dependence follows the usual Yosida function⁸⁰. We notice that the actual observed value of $\Delta K(T \rightarrow 0)$ is quite small³¹⁻³³ compared with this ideal one due to the unknown reason characteristic to heavy Fermion superconductors.

As for the H -dependence of $\Delta K(H)$ at low T is displayed in Fig. 9(b2). At the lowest H , $\Delta K(H)$ starts with $-\frac{2}{3}\chi_N$. Corresponding to the d-vector rotation phenomenon $\Delta K(H)$ gradually increases toward the normal state value. When the d-vector rotation is completed at $H_{\text{rot}} = 15\text{T}$, the polarization vector \mathbf{S} becomes perfectly parallel to the b -axis. $\Delta K(H)=0$ so that the spin susceptibility χ_s returns to χ_N ³⁵.

C. KS for $H \parallel c$ -axis

As shown in Fig. 9(c1), with decreasing T the T -dependence of $\Delta K(T)$ at low H for $H \parallel c$ -axis exhibits a drop below T_{c1} in the A_1 phase. Since \mathbf{S} points to the a -axis, $\Delta K(T \rightarrow 0) = -\frac{2}{3}\chi_N$ for this field orientation. The functional form of $\Delta K(T)$ is described by the Yosida function.

The field dependence of $\Delta K(H)$ at low T is shown in Fig. 9(c2). According to the experiments³¹⁻³³, $\Delta K(H)$

increases at the lowest H and locks to the normal state value around 8T, which is smaller than that for the b -axis, indicating that the locking energy to the crystalline lattice is weaker in this direction. This means that the original $SO(3)^{\text{spin}}$ is weakly broken due to the spin-orbit coupling.

D. KS under pressure

It is noteworthy to interpret the KS experiments under pressure $P = 1.2\text{GPa}$ by Kinjo et al³⁶ for $H \parallel b$ -axis to check the overall consistency of our scenario. According to them, as lowering T , $\Delta K(T)$ is unchanged below T_{c1} (see Fig. 19(b3) in Appendix C) where they measure KS along the T axis). Upon further lowering T , it starts decreasing below T_{c2} , and simultaneously the resonance width is broadened. At first sight, it seems unphysical: The low T phase deliberately loses the Zeeman energy since the high T phase is the most stable one by attaining \mathbf{S} parallel to the b -axis.

This paradox can be understood as follows: Since the A_1 phase has the spin polarization $\mathbf{S} \parallel b$ -axis, $\Delta K(T)$ should be unchanged below T_{c1} as observed. Thus the A_1 phase as the high T state has the order parameter Δ_{\uparrow} where the spin quantization axis must be the b -axis. Upon entering the A_2 phase as the low T state whose spin polarization is opposite to it below T_{c2} . Namely the A_2 phase has the order parameter Δ_{\downarrow} . $\Delta K(T)$ must decrease because the spin polarization \mathbf{S} points to the antiparallel direction relative to the applied field. This situation is exactly same as in the $H \parallel a$ -axis case at the ambient pressure. The concomitant resonance width broadening is fully consistent with the spin texture formation in the mixture of the A_1 and A_2 phases⁸⁸.

Thus the results are important in the following points:

(1) The high T phase of A_1 is originally inherited from the A_2 phase under the ambient pressure where the spin polarization points to the opposite direction of the applied field as mentioned above. As pressure increases, this phase becomes the low T phase after passing the critical pressure $P_{cr}=0.14\text{GPa}$ at which two phases cross each other⁴⁵. Thus above P_{cr} the high T phase has the spin polarization \mathbf{S} directed to the applied field.

(2) The resonance width in A_1 is narrow because all spin polarizations for Copper pairs are parallel. Since the low temperature phase A_2 is mixed by the A_1 phase, the spin polarization forms a spin texture, thus making the resonance width wider⁸⁸.

VI. DISCUSSION

A. Spin-singlet scenario

It may be instructive to examine the possibility of the spin-singlet scenario from both positive and negative sides.

(1) The observed H_{c2} for all three principal directions exceeds by far the Pauli paramagnetic limiting field. This difficulty for the spin-singlet scenario may be circumvented by considering the cancelation field due to induced localized moment. This avoiding Pauli limiting effect was discussed successfully in connection with CeRh_2As_2 ²⁷.

(2) The KS decreases for all three principal directions are obviously explained by a spin-singlet pairing. However, it should be noted that the KS values are not equal expected for the spin-singlet scenario.

(3) Although the time reversal symmetry either preserved or broken is under debate^{53,54,57}, it is easy to imagine that the simplest spin-singlet s -pairing is realized when the former is the case.

(4) The gap symmetry is also under discussion whether it is a nodal gap^{55,56,58} or a full gap⁵⁹. If the latter is true, the simplest spin-singlet s -pairing is most possible.

(5) There are reports^{1,65} to support ferromagnetic fluctuations which are believed to be favorable for the spin-triplet pairing formation, making the spin-triplet scenario less possible. The reported antiferromagnetic fluctuations¹⁸⁻²⁰ and incommensurate spin-density-wave long-range order⁸⁹ under pressure may be favorable for higher angular momentum pairing other than the simple s -wave one.

(6) The multiple phase diagrams under ambient and applied pressures are most difficult to explain in terms of the spin-singlet scenario unless accidentally different phases are nearly degenerate. Generically the spin-triplet pairing has various degeneracies in its spin space. In particular within our weak-spin orbit case the $SO(3)^{\text{spin}}$ has many degenerate phases because of the rich internal degrees 3×2 of spin freedom.

B. DOS mystery

We show the DOS $\gamma(H)$ evolutions^{82,84,90} under fields in Fig. 10. For $H \parallel b$ -axis, the normal state $\gamma(H)$ is displayed by the filled red dots and the empty red dots are in the superconducting state. It is seen from this that the SC $\gamma(H \parallel b)$ reaches the normal DOS γ_N around $H \sim 21\text{T}$ by extrapolating linearly to higher H where the A_1 phase ends, denoted by $H_{c2}(A_1)$. Above this field, the A_2 becomes reappearing (see Figs. 2(a) and (c)). Thus the DOS for the A_2 must be supplied by some subsystems other than the conduction electron subsystem. Since the normal state DOS denoted by the filled red dots increases beyond $\gamma_N = 120 \text{ mJ/K}^2\text{mol}$ which is supplied from the magnetic subsystem, this extra-DOS indicated by $\gamma(A_2)$ (the green arrow in Fig. 10) now available for the A_2 phase to reappear above $H=21\text{T}$. Otherwise, it is impossible to reappear because the normal DOS γ_N is exhausted by the A_1 phase when H reaches $H_{c2}(A_1)$.

As denoted by the red arrows in Fig. 10 estimated by the specific heat jumps under fields²³ the DOS for the A_2 phase exactly corresponds to these extra-DOS supplied by the magnetic subsystem (see Appendix D for details

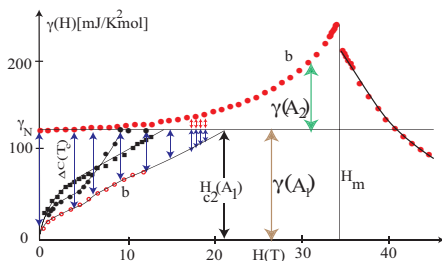


FIG. 10: $\gamma(H)$ in the normal state indicated by the filled red dots for $H \parallel b$ -axis⁸². $\gamma(H)$ in the superconducting state⁹⁰ indicated by the empty red dots and its extrapolation by the black curve. It reaches γ_N at 20T at which the A_1 state disappears. The extra DOS indicated green arrow denoted by $\gamma(A_2)$ coming from the enhanced DOS while DOS $\gamma(A_1)$ for the A_1 phase occupies the whole γ_N . The black and red arrows denoted by $\Delta C(T_c)$ show the $\gamma(H)$ estimated by the specific heat jump data.

on how to evaluate those arrows). Thus it is clear that the A_2 phase only exists near H_m where the enhanced DOS beyond γ_N is available.

As shown in Fig. 20 in Appendix D, the enhanced DOS region beyond γ_N is much wider for $\theta = 28^\circ$ than that for $\theta = 0^\circ$, namely $H \parallel b$ -axis. We denote this field region $\gamma(H) > \gamma_N$ as a function of θ in Fig. 5. Within this band, the A_2 phase can exist. This is a necessary condition for the A_2 phase to reappear above $H > H_m$. Therefore, in principle the A_2 phase can persist along $H > H_m(\theta)$, but in UTe_2 another necessary condition coming from H_{c2}^{AUL} prevents it from attaining the higher H_{c2} . On the other hand, in URhGe the reentrance A_2 phase persists up to higher angles φ measured from the b -axis as seen from Figs. 17 and 18 in Appendix C.

Here there is a mystery that is not solved: there is no available DOS for the low field A_2 phase expected below a few T since the available normal DOS is exhausted by the A_1 phase. One possibility to resolve it is to assume that the low field A_2 phase uses a small portion of the normal DOS. If it is true, we may understand that at T_{c2} there is no detectable specific heat jump.

C. Hints for the second transition T_{c2} at $H=0$ under ambient pressure

1. $T_1(T)$ anomaly

According to Matsumura, et al⁹¹, $1/T_1(T)$ on ¹²⁵Te-NMR under $H \parallel b$ -axis exhibits an anomalous rise below 0.5K for $H=0.35\text{T}$ and 0.65T , but not for 3T and 5T which show a monotonous decrease upon further lowering T . These anomalous rises in $1/T_1(T)$ suggest the appearance of the additional DOS corresponding to $\sim 0.2\gamma_N$ ⁹¹. Thus we may regard it as $T_{c2}=0.5\text{K}$ since the building-up extra-DOS comes from the second transition to newly

form of the gap edge singularity at $E = \pm\Delta_\uparrow$. This experiment⁹¹ also suggests that the small pocket region in the H - T phase diagram vanishes around $H_{c2}(A_2)=3\text{T}\sim 5\text{T}$ as indicated in Fig. 2(d).

2. $H_{c1}(T)$ anomaly

It is seen from the data⁹² that the T dependences of H_{c1} exhibit anomalous upward changes for all field directions, in particular, $H \parallel c$ -axis is eminent. Naive extrapolation of this anomaly may start around $T_{c2}=0.5\text{K}$. This kind of $H_{c1}(T)$ anomalies is also observed by Paulsen et al⁹³. Since the applied fields are around a few mT, those measurements suggest that the phase transition at $T_{c2}=0.5\text{K}$ may occur at $H=0$.

3. $\gamma(H)$ anomalies

As displayed in Figs. 10 and 20, it is seen that all $\gamma(H)$ curves in the SC state⁹⁰ exhibit anomalies around a few T. Especially $\gamma(H \parallel a)$ is eminent with a sharp kink at 4T. Those anomalies are consistent with the idea that the small pocket regions for the A_2 phase exist in the H - T phase diagrams with $H_{c2}(A_2)=4 \sim 6\text{T}$, depending on the field orientations as displayed in Figs. 2(c) and (d).

VII. CONCLUSION AND SUMMARY

1. Conclusion

We have extended our theoretical efforts toward a complete understanding of the pairing symmetry in UTe_2 . In particular, we have refined our construction work of the peculiar phase diagram for $H \parallel b$ -axis. The present work is motivated by the recent several remarkable experimental progresses using high-quality samples with $T_c=2.1\text{K}$, including the newly found fourth internal line²¹ with an almost horizontal slope going into the tetra-critical point in the $H \parallel b$ -axis together with the positive sloped H_{c2} departing from it. This improved procedure to reconstruct the b -axis phase diagram leads us to obtain the off-axis phase diagrams with a record-high H_{c2} in a consistent manner. These remarkable phase diagrams are successfully reproduced here by assuming a nonunitary state with equal spin pairs whose split transition temperatures are tuned by the underlying magnetization $M_b(H)$. This theoretical framework also explains the Knight shift experiments consistently³⁰⁻³⁶ by introducing the concept of the d-vector rotation⁸⁸ occurring at the tetra-critical point.

Within this framework on the minimal assumptions we have accomplished the following in this paper:

(1) According to Sakai et al²¹, they identified the three phases LSC, MSC and HSC for the $H \parallel b$ -axis. These

TABLE I: Characterizations of the four phases for $H \parallel b$

phase	ΔK	d-vector	vortex core (flow)	width*
LLSC	decrease	spin texture	soft(flux flow)	wide
LSC	decrease	$\mathbf{d} \parallel \mathbf{H}$ (uniform)	hard(pinned)	wide
MSC	decreas	spin texture	soft(flux flow)	wide
HSC	unchange	$\mathbf{d} \perp \mathbf{H}$ (uniform)	hard(pinned)	narrow

*width: NMR resonance width

phases are characterized in Table I. In addition to the three phases the fourth phase LLSC as the lowest H phase is proposed here. The Table I includes the character associated with the vortex core structures in each phase, in particular whether it is pinned in crystal lattices or easy depinned, exhibiting the flux flow under the applied current. It also describes the width of the NMR resonance spectrum, which matches with the observed characteristics^{30,36}.

(2) In addition to the peculiar phase diagram for $H \parallel b$ -axis, we have shown that the high field A_2 phase is reentrant when the field orientation is tilted from the b -axis to the c -axis and from the bc -plane toward the a -axis, achieving extremely high H_{c2} . This is caused by the screening effect of the external field by the internal field due to the localized 5f moment M_b along the b -axis, which exhibits the meta-magnetic transition. This explains the truly multiple phases in this system.

(3) We have pointed out similarities and differences from the sister materials URhGe in the phase diagram, maintaining the same scenario based on the nonunitary equal-spin pairing.

(4) Under pressure the observed multiple phase is demonstrated to be connected to the multiple phase in ambient pressure. This allows us to paint out the whole phase diagrams in a unified viewpoint.

(5) We have analyzed the DOS data to show that the high field A_2 phase as HSC is needed for the extra DOS, which is supplied from the localized magnetic subsystem. Thus for the A_2 phase to appear the extra DOS associated with the meta-magnetic transition is indispensable, hinting at the novel pairing mechanism.

(6) We have explored thoroughly the KS experiments by NMR for all field orientations and under pressure in a consistent manner and predicted the KS behaviors which are not done yet.

To strengthen our argumentation, we have to back it up in several aspects:

(1) Since our arguments are qualitative or semi-quantitative, we need more microscopic calculations based on a microscopic Hamiltonian. This includes the H_{c2} evaluation quantitatively based on band calculations, giving the realistic values of the anisotropy and accurate position of the tetra-critical point.

(2) Microscopic computations are needed to understand the dynamical processes of the formation and nucleation for spin textures to accurately describe the d-vector rotation phenomena by extending our microscopic Eilen-

berger theory⁸⁸ or Bogoliubov-de Gennes theory⁹⁴.

(3) Although it is a notoriously difficult question and so far no one answers reasonably, the origin of the pairing mechanism of this kind of particular superconducting state must be addressed. Here we have tried to extract some hints related to this fundamental question which might give clues. For example, as mentioned in Sec. VI in order to produce the high field A_2 phase above H_m the extra DOS must be supplied from the magnetic subsystem whose internal degrees of freedom associated with the Kondo screening is liberated under strong external fields by more and more localizing the 5f moments. On the other hand, the low field A_2 phase as LLSC expected to appear at T_{c2} under ambient pressure and T_{c1} under applied pressure seems to hold only tiny entropy compared with the A_1 phase with holding the almost full DOS $\gamma_N=120\text{mJ/mol K}^2$, not sharing half- and half-DOS for each. It seems quite puzzling at this moment because the spin-down system Δ_{\downarrow} overwhelms the spin-up system Δ_{\uparrow} .

(4) The pairing mechanism must be related to the underlying magnetism because the present system is governed by the field-tuned 5f magnetic moment. The recent discovery of the long-range incommensurate spin-density-wave under high pressure⁸⁹ and antiferromagnetic fluctuations¹⁸⁻²⁰ under ambient pressure may indicate a hint for the pairing glue. More broadly, the competing phase between superconductivity and magnetism belongs to more general topics not only in heavy Fermion materials⁹⁵⁻⁹⁸, but also in high T_c cuprates^{99,100}.

(5) In the present paper we do not touch upon the gap structure because it is not directly relevant for our phase diagram construction. But its determination is essential to finally pin down the proper pairing state because the spin part and orbital part of the order parameter must be mutually consistent. At this moment there are conflicting opinions on the gap structure, either nodal or full gap. To resolve it, we need further efforts both theoretically and experimentally. Some of these tasks are underway.

Finally, we wish to list up the experimental works to be urgently performed:

(A) According to the present scenario⁸⁸, the vortex core in the high field A_2 phase for $H \parallel b$ -axis contains a genuine spinless Majorana zero-energy mode. This can be detected by STM-STs via the local density of states measurements¹⁰¹.

(B) The spin textural changes associated with the d-vector rotation, whose precise field and temperature region is identified in the present paper, can be also observed by small angle neutron scattering (SANS) experiments.

(C) The detailed $\gamma(H)$ measurements in higher fields for the $H \parallel b$ -axis is necessary for clarifying the DOS mystery mentioned above.

(D) The experimental check on whether or not the second transition at $T_{c2}=0.4\sim 0.5\text{K}$ described in this paper is needed by using high-quality samples with $T_c=2.1\text{K}$. The thermodynamic anomaly is expected to be very small,

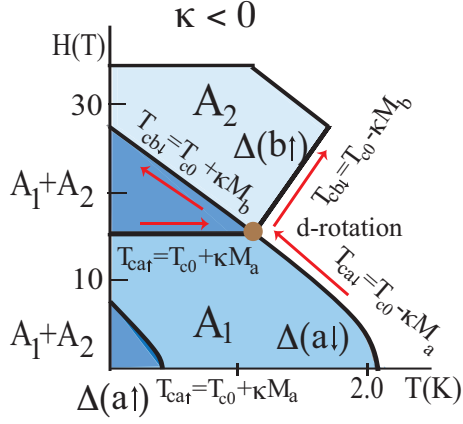


FIG. 11: The characterization of the order parameters and the transition lines for the phase diagram in H - T plane for $H \parallel b$ -axis.

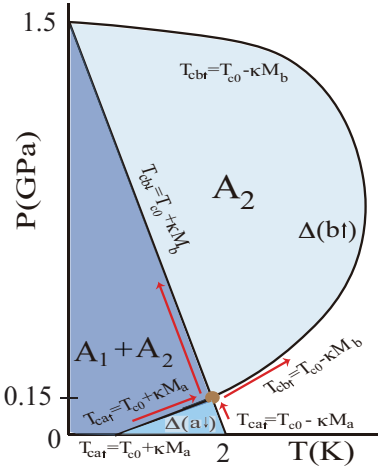


FIG. 12: The characterization of the order parameters and the transition lines for the phase diagram in P - T plane.

thus high-resolution experiments are indispensable. According to a recent paper¹⁰², it is pointed out that the second transition in a nonunitary state can be small because of the presence of $\mathbf{d} \times \mathbf{d}^*$.

(E) To precisely determine the gap structure as for the nodal topology, point or line, or full gap and its reciprocal-space position, the angle-resolved specific heat¹⁰³ or thermal-conductivity measurements are highly desired.

2. Summary

To facilitate future experiments, it may be instructive to summarize the identified pairing states on the phase diagrams for $H \parallel b$ -axis and under pressure. On the phase diagram for $H \parallel b$ -axis, which is derived early in Figs. 1

and 2(c) the relevant order parameters are described in Fig. 11. Here we have introduced the notation for the order parameters, such as $\Delta(a \downarrow)$ where the quantization axis of the spin direction is specified and the transition temperatures are specified, such as $T_{ca \downarrow} = T_{c0} - \kappa M_a$, indicating that $\Delta(a \downarrow)$ appears at this temperature governed by M_a . The red arrows at the tetra-critical point denote the reconnections of the transition lines, namely $T_{ca \downarrow} = T_{c0} - \kappa M_a$ at 2K ($T_{ca \uparrow} = T_{c0} + \kappa M_a$) reconnects to $T_{cb \uparrow} = T_{c0} - \kappa M_b$ ($T_{cb \downarrow} = T_{c0} + \kappa M_b$) at TCP where the d -vector rotates. Thus the low field phase A_1 (the high field phase A_2) is characterized by the order parameter $\Delta(a \downarrow)$ ($\Delta(b \uparrow)$).

We notice that at TCP the four transitions meet together. They are all degenerate, allowing them to freely reconnect so as to be maximally beneficial for them. In fact for $\Delta(b \uparrow)$ the transition line $T_{cb \uparrow} = T_{c0} - \kappa M_b$ is most beneficial because the diamagnetic effect is absent and the transition temperature can strongly increase as $M_b(H)$ grows toward higher fields in our case of $\kappa < 0$. These identifications are fully consistent with the Knight shift experiments.

Under pressure the P - T phase diagram is shown in Fig. 12. The similarity between Figs. 11 and 12 is noticeable: Namely the high pressure and high temperature phase corresponding to the A_2 phase with $\Delta(b \uparrow)$ changes into the mixture phase of $A_1 + A_2$ phase upon cooling where $\Delta(b \downarrow)$ appears at $T_{cb \downarrow} = T_{c0} + \kappa M_b$. This identification of the spin structure of the order parameters is consistent with the Knight shift experiment by Kinjo et al³⁶ under $P = 1.2$ GPa. At the tetra-critical point $P \sim 0.15$ GPa the d -vector rotation must occur.

Acknowledgments

The author sincerely thanks K. Ishida, and S. Kitagawa for sharing unpublished results, which motivates the present project. He is indebted to D. Aoki, and R. Movshovich for showing their data prior to publication and T. Sakakibara, S. Kittaka, Y. Shimizu, A. Miyake, Y. Tokunaga, H. Sakai, M. Yamashita, T. Shibauchi, K. Hashimoto, K. Ishihara, and S. Imajo for enlightening and fruitful discussions. This work is supported by JSPS KAKENHI, Grant No. 21K03455 and No. 17K05553. A part of this work was performed during stay at the Aspen Center for Physics, which is supported by National Science Foundation grant PHY-2210452.

Appendix A: Phase diagrams for $T_c=1.6$ K samples

The samples with $T_c=1.6$ K exhibit no indication for the double transition at T_{c2} at the ambient pressure and $H=0$. Note that all the indications of the second transition T_{c2} in sec. VI C come from the samples with $T_{c2}=2$ K^{30,90,92}. This is caused by the large residual DOS comparable to $0.5\gamma_N$, which ultimately excludes the A_2

phase from realizing by pushing T_{c2} to a negative value. We remark that the new samples with $T_c=2.1\text{K}$ have no such residual DOS. Other various eminent features discussed in the main text remain intact even in these samples with $T_c=1.6\text{K}$. In particular, for $H \parallel b$ -axis unusual phenomena, such as the positive slope in H_{c2} above 15T, the successive transition under fields and the high field reentrant SC for the field orientations along θ are observed in the low-quality samples. Thus it is important to check whether or not the present theoretical framework can explain these prominent features.

1. Construction of the phase diagram for $H \parallel b$ -axis

We employ the same method to construct the phase diagram for $H \parallel b$ -axis as in the main text except for $T_{c2} < 0$, thus we use $\kappa = 3.9\text{K}/\mu_B$. As shown in Fig. 13(b) which is identical with Fig. 1(b), the magnetization curve $M_b(H)$ is plotted by the red line and the green line indicates H_{eff} for the A_2 phase. The A_1 phase is essentially unchanged in the case of the main text, namely it vanishes at $H=22\text{T}$ corresponding to their orbital limiting field $H_{c2}^{\text{orb}}(A_1)$ (see the gray band) because $H_{\text{eff}} = H_{\text{ext}}$ is unscreened.

In contrast, the A_2 phase starting with the negative temperature $T_{c2} < 0$ survives in much higher fields because H_{eff} denoted by the green line comes back within the allowed region denoted by the blue band above the d-vector rotation field $H > H_{\text{rot}}$. Thus it appears above $H_{\text{rot}}=15\text{T}$ first (see in Fig. 13(a)) and vanishes at the meta-magnetic transition $H_m=34\text{T}$ above which as indicated by the green line it is outside the allowed region.

The main different from the case of $T_{c2} > 0$ lies in the fact that until the T_{c2} becomes positive, the A_2 phase does not appear and even when it becomes positive, it never appears because $H_{\text{eff}}(A_2)$ is outside the allowed region below H_{rot} (see the black straight line for $H = H_{\text{ext}}$ in Fig. 13(b)).

We show the A_2 (left) and A_1 (right) phases separately in the top panel of Fig. 14. It is clear that the A_2 phase is isolated and has a positive slope while the A_1 phase has a simple conventional $H_{c2}(T)$ form. The overlapping region of the two phases gives rise to the mixture phase of A_1 and A_2 phases and the tetra-critical point shown in the lower panel of Fig. 14. Note that in contrast with the main text with $T_{c2} > 0$ (see Fig. 2), other internal transition line is absent and the dotted lines are not realized.

2. Phase diagram from $H \parallel b$ -axis to c -axis

We construct the phase diagram for the field direction tilted from the b -axis toward the c -axis by $\theta = 35^\circ$. As shown in the left panel of Fig. 15 by the red curve, just above H_m , H_{eff} becomes inside the allowed region denoted by the vertical band which is defined by

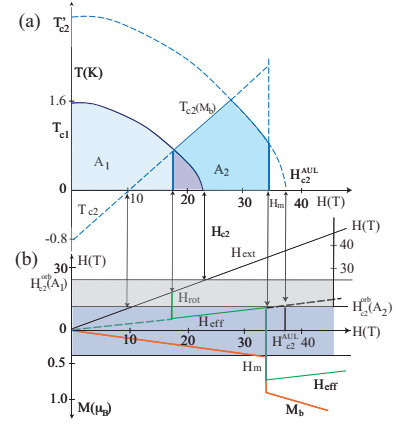


FIG. 13: Construction of the phase diagram for $H \parallel b$ -axis when $T_{c1} < 0$. The lower panel shows the magnetization curve of $M_b(H)$ by the red line. The green line is H_{eff} as a function of H where the dotted lines are not realized. The two horizontal bands exhibit the allowed regions $H_{c2}^{\text{orb}}(A_1)$ and $H_{c2}^{\text{orb}}(A_2)$ for the A_1 and A_2 phases respectively. Upper panel: The constructed phase diagram $H \parallel b$ -axis in the T - H plane. T_{c2} starts at the negative T and becomes positive at 10T, keeping up until meeting the curve starting from $H_{c2}^{\text{orb}}(A_1)$. The A_1 phase with $T_{c1}=1.6\text{K}$ disappears at $H=23\text{T}$. Above H_{rot} the A_2 phase appears and vanishes at H_m .

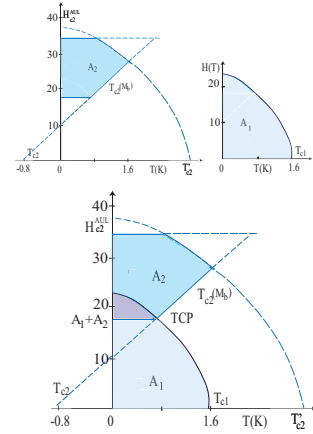


FIG. 14: The upper panel shows the phase diagram for the A_2 phase (left) and the A_1 phase (right) in the H - T plane. The former does not contain the A_2 phase in the low T and H region. The lower panel shows the total phase diagram combined with the two phases. The four second order lines meet at 15T, constituting the tetra-critical point. The region around 20T consists of A_1 and A_2 , giving the mixture phase.

$\pm H_{c2}^{\text{orb}}(\theta = 35^\circ)$. Thus the A_2 phase, shown in the right hand side of Fig. 15, appears above H_m , a situation same as in the main text. Here the straight dotted line starting at $T_{c2} < 0$ is never realized, so there is no further internal transition line.

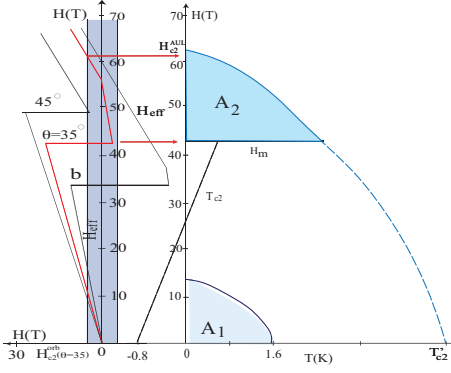


FIG. 15: Phase diagram for $H \parallel \theta = 35^\circ$. The left side panel shows H_{eff} by the red line with the vertical allowed region bound by $H_{c2}^{\text{orb}}(\theta = 35^\circ)$. The A_2 phase appears above H_m and below H_{c2}^{AUL} . T_{c2} is not realized until it hits H_m .

Appendix B: Comparisons with URhGe

It is instructive to compare the above analysis on UTe_2 with URhGe ^{26,41–43} because they have similar phase diagrams in common under the field direction for the magnetic hard b -axis. We construct the phase diagram for $H \parallel b$ -axis in URhGe shown in Fig. 16. The construction procedure is the same as in the main text: Since $T_{c2} < 0$ is situated deep in the negative side, the A_2 phase appears when the magnetization M_b exhibits a jump at H_R where the magnetic moment rotates from the magnetic easy c -axis. H_R corresponds to the meta-magnetic transition H_m before. We have chosen the following parameters to construct the phase diagrams here and throughout: $T_{c2} = -0.6\text{K}$ under the observed transition temperature $T_{c1} = 0.22\text{K}$. κ is determined by the splitting of $T_{c1} - T_{c2} = 2\kappa M_c$ with the spontaneous moment $M_c = 0.4\mu_B$, yielding $\kappa = 1.0\text{K}/\mu_B$. Together with $\alpha_0^b = 40.5\text{T/K}$, we use $H_{c2}^{\text{orb}} = \alpha_0^b |T_{c2}| = 24.3\text{T}$.

The magnetization jump greatly reduces the external field as depicted in the left side panel. This results in that the isolated A_2 phase appears above the A_1 phase stabilized only in lower fields. H_{c2}^{AUL} determined by H_{eff} is comparable to the upper limit of the extra DOS region ($\gamma(H) > \gamma_N$) indicated by the blue arrow along the H -axis of the left panel. These two factors yield the upper bound in the A_2 phase. It is rather remarkable to see that the magnetization curve of $M_b(H)$ indicated by the dots in the right panel forms the lower part of the reentrant A_2 phase. This proves that the expression $T_{c2} = T_{c0} + \kappa M_b$ is correct.

By continuing the same arguments, we can construct the phase diagrams when the field direction is tilted from the b -axis toward the other hard a -axis by the angle φ . As displayed in the left hand panel of Fig. 17 where H_{eff} is shown for the selected angles. To construct this figure, once the value κ is fixed we need:

(1) The magnetization curves of the $M_b(H)$ component

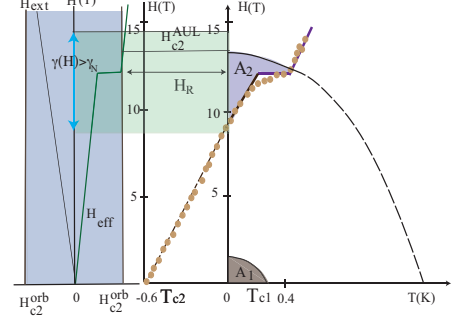


FIG. 16: Construction of the phase diagram for $H \parallel b$ in URhGe . The left side panel: H_{eff} is shown in the green line relative to the external field H_{ext} denoted by the black line, which runs out at H_{c2}^{AUL} from the allowed region set by H_{c2}^{orb} . The blue arrow indicates the region $\gamma(H) > \gamma_N$, which limits the A_2 phase to appear. The right side panel: H - T phase diagram obtained. $T_{c2} = -0.6\text{K}$ starts from the negative value according to $T_{c2} = T_{c0} + \kappa M_b(H)$, which becomes positive at 9T and jumps at the moment rotation field H_R . The A_2 phase appears around it, isolated from the A_1 phase in low H and T region. This phase diagram is similar to that in UTe_2 , having a portion $\frac{dH_{c2}}{dT} > 0$.

for those angles φ which are done by taking the projection $M_b(H)$ onto the external field direction. $M_b(\varphi = \pi/2)$ coincides with $M_c(H)$. This procedure is experimentally verified⁸².

(2) $M_b(\varphi)$ starting from T_{c2} at the zero-field yields $H_{\text{eff}} = H + \alpha_0 \kappa M_b(\varphi)$, which is shown in the right hand panel.

(3) The initial slope α_0 depends on the angle φ , but the H_{c2} anisotropy from the b -axis to a -axis is weak, thus we neglect it. Note that this anisotropy was strong in UTe_2 which greatly influences the phase diagrams around $\theta \sim 40^\circ$ to attain the maximal $H_{c2}(\theta)$ there.

It is now seen from Fig. 17:

(A) Since nearly all H_{eff} for various φ are well within the allowed region up to the highest field, meaning that H_{c2}^{AUL} is not effective here. This is different from that in UTe_2 . Instead, the upper limit of the A_2 phase is limited by the extra DOS with $\gamma(H) > \gamma_N$, whose field regions are assumed to be constant here to be consistent with the experimental data. Namely the width of the field region for $\gamma(H) > \gamma_N$ is a constant centered around $H_R(\varphi)$. This assumption should be checked experimentally. Indirect supporting evidence comes from the pressure experiment by Miyake et al⁴³, showing that the shape of the reentrant A_2 phases under pressure simply shifts without changing their width along the field direction, which is consistent with our assumption.

(B) The magnetization jump always occurs when the magnetization $M_\varphi(H)$ reaches at a certain value $\sim 0.4\mu_B$ for all φ . This is consistent with the experimental observation $H_R(\theta) \propto 1/\cos\varphi$. This means that in the right hand panel in Fig. 17 the jump point for each φ aligns

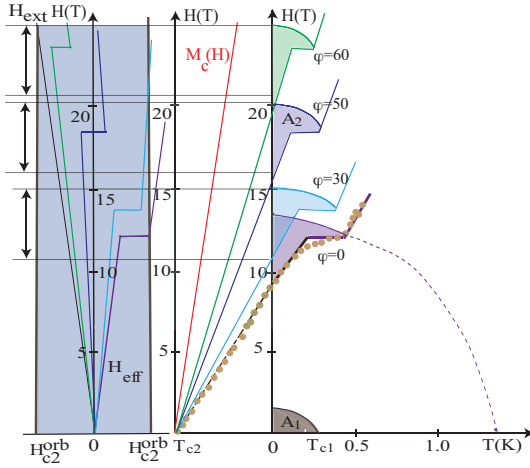


FIG. 17: Construction of the phase diagrams under varying the angle φ measured from the b -axis toward the a -axis. The left side panel: H_{eff} for $\varphi = 0^\circ, 30^\circ, 50^\circ, 60^\circ$. The three arrows indicate the field region for $\gamma(H) > \gamma_N$ which limits the A_2 phase to appear. The right side panel: H - T phase diagram obtained where $T_{c2} = T_{c0} + \kappa M(\varphi)$ with $M(\varphi)$ depicted there for each φ started from T_{c2} . The reentrant A_2 phase persists up to higher angles, sticking with H_R .

vertically parallel to the H -axis. This guarantees the existence of the reentrant A_2 phase to always appear just around their H_R . This is the reason why it is accompanied by H_R up to a higher angle φ .

As shown in Fig. 18, the A_2 phase forms a band centered around H_R at least up to $\varphi = 50^\circ$. This situation is quite different from that in UTe_2 shown in Fig. 5. In short, in the latter case the two factors H_{c2}^{AUL} and the extra DOS region compete with each other to confine the A_2 phase to a narrow angle region. However the attained field of H_{c2} is far high because the magnetization jump is bigger $0.5\mu_B$ in UTe_2 than $\sim 0.1\mu_B$ in URhGe .

Appendix C: Multiple phase diagrams under pressure

We have postulated the existence of the second transition $T_{c2}=0.4\text{K}$ at $H=0$ to construct the phase diagram for the $H \parallel b$ -axis. It implies that the H - T phase diagrams for all field directions should consist of multiple phases in general. Here we demonstrate that this assumption is quite natural when analyzing the phase diagrams under pressure. Moreover, the third phase A_0 , which is hidden so far appears to exist, completing the three component scenario based on $\text{SO}(3)^{\text{spin}}$ introduced previously.

In Fig. 19, we analyze the H - T phase diagrams for all principal field directions; a , b and c -axes under pressure⁴⁵⁻⁵¹. It is seen from Fig. 19 that:

- (1) It is obvious that all phase diagrams consist of the multiple phases, independent of P and field orientations.
- (2) The multiple phases are classified by the three phases,

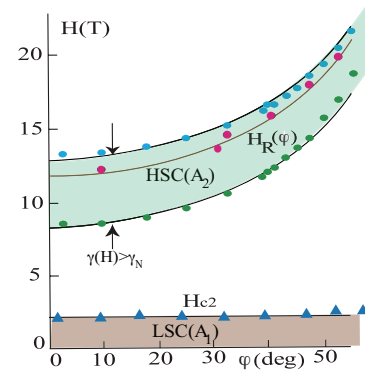


FIG. 18: The constructed phase diagram in H - φ plane. The reentrant $\text{HSC}(A_2)$ is within the light green band around $H_{\text{rot}}(\varphi)$ denoted by a thin black curve with red dots. The blue, and green dots and triangle symbols are experimental data for superconducting transitions. The two arrows indicate the field region for $\gamma(H) > \gamma_N$. $\text{LSC}(A_1)$ is almost isotropic against φ .

A_1 , A_2 , and A_0 . There is no further phase existed in this analysis. This is consistent with our three component scenario.

(3) The A_0 phase is somewhat hidden because so far at $H = 0$ there is no direct experimental report to third transition T_{c3} while the double transition T_{c1} and T_{c2} are confirmed by several experiments mentioned above. However, if we look carefully at the data for $H \parallel a$ -axis in Figs. 19 (a1), (a2), and (a3), it is understood that there must be an additional phase in high fields, namely the A_0 phase indicated by green, which is systematically evolving under P .

(4) As for the field direction b -axis shown in Figs. 19 (b1), (b2), and (b3), we see that the A_2 phase starting at T_{c2} quickly disappears at lower fields. In contrast, the high temperature A_1 phase starting at T_{c1} exhibits a strong rise, and a positive slope in the middle field region toward H_m indicated by horizontal dotted lines. The other dotted lines there from T_{c2} toward the tetra-critical points are not realized. The existing data points are completely exhausted by those analyses, so we understand that there are no positive sloped internal phase transition lines inside the A_1 phase.

(5) This assignment is completely consistent with the constructed b -axis phase diagram shown in Figs. 1, 2, 3, and 4 in the ambient pressure. Therefore, as a function of P , including the ambient pressure the phase diagrams are continuously evolving.

(6) We notice that the small pocket regions for the A_2 phase around the origin always exist, independent of P and field directions, a situation quite similar to the ambient pressure as shown in Figs. 2(c) and (d).

To conclude this section, through the examinations of the data under pressure, it is natural to assume that in

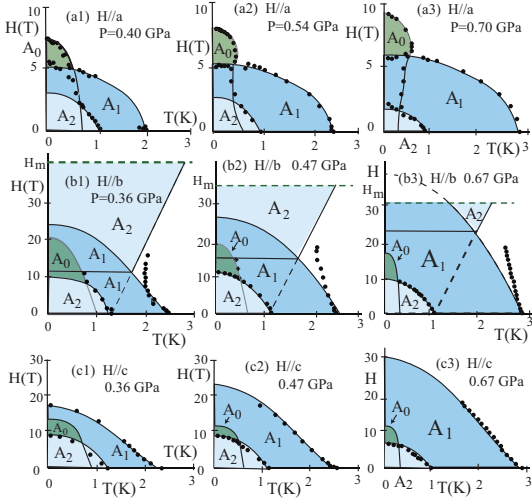


FIG. 19: Phase diagrams under pressure^{45–51}. Each row corresponds to the field orientations *a*-axis, *b*-axis, and *c*-axis. Each column corresponds to approximately the same pressure, low, middle, and high pressures. The black dots are experimental data points. The identified phases for A_1 , A_2 , and A_0 are colored differently. The produced phase diagrams capture the experimental data points. Systematic evolutions of the three phases are seen under pressures and field orientations.

the ambient pressure T_{c2} exists at $H=0$ for $T_c=2.1\text{K}$ samples. The A_2 phase at low T and H occupied a small pocket area in the H - T phase diagram shown in Figs. 1~4. This is in contrast with $T_c=1.6\text{K}$ samples where T_{c2} is absent, or negative because the large residual DOS wipes out the A_2 phase to appear.

Appendix D: Available DOS for A_2 phase in high fields –A hint for pairing mechanism–

Here in Fig. 20 we refer to the experimental data for the normal DOS for the *b*-axis and $\theta = 28^\circ$ by Miyake et al⁸⁴. The DOS or $\gamma(H)$ enhancement occurs associated with the meta-magnetic transition at H_m . Above H_m , as a function of H , $\gamma(H)$ quickly decreases. Comparing the field regions, in which $\gamma(H) > \gamma_N$ indicated by the horizontal arrows are far wider for the $\theta = 28^\circ$ case than that in the *b*-axis case.

On the other hand, $\gamma(H)$'s in the superconducting state for the three *a*, *b*, and *c* axes⁹⁰ are also shown in Fig. 20 by the black dots. When $\gamma(H)$ reaches $\gamma_N=120\text{mJ/molK}^2$ for *a* and *c*-axes, the system becomes normal. Extrapolating the *b*-axis data linearly to higher fields, it reaches γ_N around 22T or so at which the A_1 phase disappears as seen from Fig. 2 simply because the A_1 phase exhausts its available DOS, e.g. γ_N . Thus for the A_2 phase to reappear around that field region, it is necessary to be available for the extra DOS, oth-

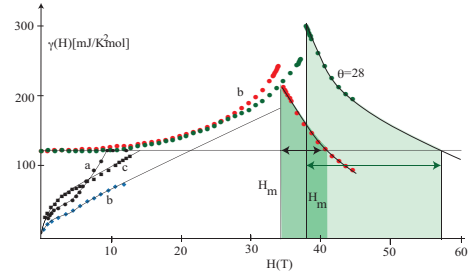


FIG. 20: Field dependences⁸⁴ of the normal DOS $\gamma(H)$ for $H \parallel b$ -axis and tilted by $\theta = 28^\circ$. Both show the enhancements toward H_m and decreases. The colored regions ($H > H_m$) with the arrows show the enhancement exceeded above $\gamma_N = 120\text{mJ/K}^2\text{mol}$ and differ for the two cases where the latter is far wider than the former. The low field data below γ_N show the superconducting $\gamma(H)$ for three orientations⁹⁰.

erwise, there is no usable DOS for the A_2 phase or no room for the A_2 phase. Then as mentioned above according to the DOS enhancement associated with the meta-magnetic transition, the extra DOS becomes available for the A_2 phase around H_m . This field interval is necessary for the A_2 phase to reappear in high fields for $\theta \sim 35^\circ$ as explained in the previous section. Note that for $H \parallel b$ -axis this field interval is too narrow for the A_2 phase to reappear above H_m even though $H_{c2}^{\text{AUL}}(\text{lower}) < H_{\text{eff}} < H_{c2}^{\text{AUL}}(\text{upper})$. The enhanced DOS is quite high for $\theta = 28^\circ$ which is more than $2 \times \gamma_N$, making the extrapolated $T'_{c2} \sim 6\text{K}$ so high as shown in Figs. 3 and 4. It is also noticed that in URhGe high field reentrant A_2 phase is mainly constrained by this extra DOS interval. This suggests that the pairing mechanism is closely related to the origin of the mass enhancement. The reentrant A_2 phase in URhGe is always associated with this mass enhancement region.

Appendix E: Estimate for the KS value for the *a*-axis and the Pauli paramagnetic field

The new KS value for the *a*-axis³⁰ at lower H is $\Delta K_a=4.8\%$ where the spin part of the KS $K_{\text{spin}}=1.3\%$, namely, $\Delta K_a/K_{\text{spin}}=3.7$. This evaluation is consistent with the following estimate: The induced magnetization at $H=1\text{T}$ is $M_a = -4.8\% \times 1\text{T}/3.8\text{T}/\mu_B = -0.00126\mu_B$ with the hyperfine coupling constant $A_a^{\text{hyperfine}} = 3.8\text{T}/\mu_B$ for the Te site 2. On the other hand, the Pauli paramagnetic moment M_{Pauli} at $H=1\text{T}$ is given by $M_{\text{Pauli}} = \chi_{\text{Pauli}} \times 1\text{T} = 2\mu_B^2 N(0) \times 1\text{T} = 0.003\mu_B$. Thus, $M_a/M_{\text{Pauli}} = -0.0126\mu_B/0.003\mu_B = -4.2$ where $N(0) = 120\text{mJ/molK}^2$. Both estimates yield the Knight shift value $-3.7 \sim -4.2\chi_N$. Note that contrary to this anomalously large KS, for the *b* and *c*-axes the corresponding values are the following: $\Delta K_b/K_{\text{spin}} \sim \Delta K_c/K_{\text{spin}} = -0.15$ and $M_b/M_{\text{Pauli}} = -0.13$ and $M_c/M_{\text{Pauli}} = -0.17$.

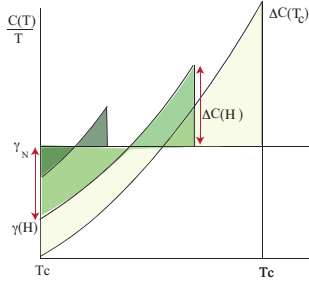


FIG. 21: The specific heat jump $\Delta C(H)$ at $T_c(H)$ under fields indicated by the red arrow. The entropy balance requires that the two triangle areas above and below γ_N must be equal, meaning that the length $\gamma_N - \gamma(H)$ is uniquely related to $\Delta C(H)$, independent of the functional form of $C(H)$.

From the observed KS value we can evaluate the Pauli paramagnetic limiting field as $H_{\text{Pauli}}^a = 2\text{T}$, which is compared with $H_{\text{Pauli}}^b = 10\text{T}$. These values are far below the observed H_{c2} for the a and b -axes. This strengthens the scenario based on a triplet pairing for UTe_2 .

Appendix F: Different estimate for the KS value for the a -axis

According to Miyake⁸⁷, the induced magnetization value associated with the A_1 phase is evaluated by a formula relative to the normal state due to the Pauli paramagnetism M_{Pauli} :

$$\frac{|\delta M|}{M_{\text{Pauli}}} = \frac{\alpha \Delta^2}{4\epsilon_F \mu_B H} \left(1 + \frac{2}{gN(0)}\right) (1 + F_0^a) \quad (\text{F1})$$

where $\alpha \sim O(1)$ is the parameter to express the degree of the electron-hole asymmetry, namely $N'(0)$ the derivative at the Fermi level $\epsilon_F (= T_K = 30\text{K})$. $gN(0)$ is the dimensionless coupling constant, assuming here 0.14. F_0^a is the Landau Fermi liquid parameter, which

we ignore. For $\Delta = 1.75T_{c1}(\text{K})$, and $H=1\text{T}$, we find $|\delta M|/M_{\text{Pauli}} = 2.2\alpha$. This is the same order of magnitude estimated in the main text.

Appendix G: Evaluation of $\gamma(H)$ from the jump of the specific heat at T_c

We can estimate $\gamma(H)$ from the specific heat jump $\Delta C(H)$ at T_c by assuming the entropy balance between the SC and the normal state as follows: As shown in Fig. 21, at $H = 0$, $\gamma(H = 0) = 0$ and $\Delta C(H = 0) = 1.43\gamma_N$ for the BCS. As H increase from zero, the jump decrease, and the residual $\gamma(H)$ increases so that both keep the entropy balance, namely the area of the upper triangle equals that of the lower triangle. Then we can derive a formula under the assumption that all the specific heat curves are scaled:

$$\frac{\Delta C(H)}{\Delta C_{\text{BCS}}} = 1 - \frac{\gamma(H)}{\gamma_N}. \quad (\text{G1})$$

Since this relation is independent of the functional form of the $C(T)$ curve and the magnitude of the jump, we can generalize it to the non-BCS cases as

$$\frac{\gamma(H)}{\gamma_N} = 1 - \frac{\Delta C(H)}{\Delta C(H = 0)}. \quad (\text{G2})$$

In fact we confirm this formula for UTe_2 by comparing the estimates $\gamma(H)/\gamma_N$ calculated by this formula with the measured values⁹⁰ as displayed in Fig. 10 where the black arrows indicates the jumps $\Delta C(T_c)$ in the $H \parallel b$ -axis²³. It is seen that they agree with each other rather perfectly. This tells us that the analysis of the specific heat jump associated with the A_2 phase in the double transition around 17T gives reliable estimates for the $\gamma(A_2)$ which are also displayed in Fig. 10 as the red arrows.

¹ Sheng Ran, Chris Eckberg, Qing-Ping Ding, Yuji Furukawa, Tristin Metz, Shanta R. Saha, I-Lin Liu, Mark Zic, Hyunsoo Kim, Johnpierre Paglione, Nicholas P. Butch, Nearly ferromagnetic spin-triplet superconductivity, *Science* **365**, 684 (2019).

² D. Aoki, A. Nakamura, F. Honda, D. Li, Y. Homma, Y. Shimizu, Y. J. Sato, G. Knebel, J.-P. Brison, A. Pourret, D. Braithwaite, G. Lapertot, Q. Niu, M. Vališka, H. Harima, and J. Flouquet, Unconventional Superconductivity in Heavy Fermion UTe_2 , *J. Phys. Soc. Jpn.* **88**, 043702 (2019).

³ D. Aoki, J. -P. Brison, J. Flouquet, K. Ishida, G. Knebel, Y. Tokunaga, and Y. Yanase, Unconventional Superconductivity in UTe_2 , *J. Phys.: Condens. Matter* **34**, 243002

(2022).

⁴ S.K. Lewin, C.E. Frank, S. Ran, J. Paglione, and N.P. Butch, A Review of UTe_2 at High Magnetic Fields, *Rep. Prog. Phys.* **86**, 114501 (2023).

⁵ R. Joynt and L. Taillefer, The superconducting phases of UPt_3 , *Rev. Mod. Phys.* **74**, 235 (2002).

⁶ J. A. Sauls, The Order Parameter for the Superconducting Phases of UPt_3 , *Adv. Phys.* **43**, 113 (1994).

⁷ K. Machida and M. Ozaki, Superconducting double transition in a heavy-fermion material UPt_3 , *Phys. Rev. Lett.* **66**, 3293 (1991).

⁸ T. Ohmi and K. Machida, Nonunitary superconducting state in UPt_3 , *Phys. Rev. Lett.* **71**, 625 (1993).

⁹ Y. Machida, A. Itoh, Y. So, K. Izawa, Y. Haga, E.

- Yamamoto, N. Kimura, Y. Onuki, Y. Tsutsumi, and K. Machida, Twofold Spontaneous Symmetry Breaking in the Heavy-Fermion Superconductor UPt_3 , *Phys. Rev. Lett.* **108**, 175002 (2012).
- ¹⁰ Y. Tsutsumi, M. Ishikawa, T. Kawakami, T. Mizushima, M. Sato, M. Ichioka, and K. Machida, UPt_3 as a Topological Crystalline Superconductor, *J. Phys. Soc. Jpn.* **82**, 113707 (2013).
- ¹¹ H. R. Ott, H. Rudigier, T. M. Rice, K. Ueda, Z. Fisk, and J. L. Smith, p-Wave Superconductivity in UBe_{13} , *Phys. Rev. Lett.* **52**, 1915 (1984).
- ¹² Yusei Shimizu, Daniel Braithwaite, Dai Aoki, Bernard Salce, and Jean-Pascal Brison, Spin-Triplet p-Wave Superconductivity Revealed under High Pressure in UBe_{13} , *Phys. Rev. Lett.* **122**, 067001 (2019).
- ¹³ Yusei Shimizu, Shunichiro Kittaka, Toshiro Sakakibara, Yoshinori Haga, Etsuji Yamamoto, Hiroshi Amitsuka, Yasumasa Tsutsumi, and Kazushige Machida, Field-Orientation Dependence of Low-Energy Quasiparticle Excitations in the Heavy-Electron Superconductor UBe_{13} , *Phys. Rev. Lett.* **114**, 147002 (2015).
- ¹⁴ J. E. Sonier, R. H. Heffner, D. E. MacLaughlin, G. J. Nieuwenhuys, O. Bernal, R. Movshovich, P. G. Pagliuso, J. Cooley, J. L. Smith, and J. D. Thompson, μ^+ Knight Shift Measurements in $U_{0.965}Th_{0.035}Be_{13}$ Single Crystals, *Phys. Rev. Lett.* **85**, 2821 (2000).
- ¹⁵ Yusei Shimizu, Shunichiro Kittaka, Shota Nakamura, Toshiro Sakakibara, Dai Aoki, Yoshiya Homma, Ai Nakamura, and Kazushige Machida, Quasiparticle excitations and evidence for superconducting double transitions in monocrystalline $U_{0.97}Th_{0.03}Be_{13}$, *Phys. Rev. B* **96**, 100505 (2017).
- ¹⁶ Kazushige Machida, Spin Triplet Nematic Pairing Symmetry and Superconducting Double Transition in $U_{1-x}Th_xBe_{13}$, *J. Phys. Soc. Jpn.* **87**, 033703 (2018).
- ¹⁷ D. Vollhart and P. Wölfle, *The superfluid phases of Helium 3*, Taylor and Francis, London, 1990.
- ¹⁸ C. Duan, K. Sasmal, M. B. Maple, A. Podlesnyak, J.-X. Zhu, Q. Si, and P. Dai, Incommensurate Spin Fluctuations in the Spin-triplet Superconductor Candidate UTe_2 , *Phys. Rev. Lett.* **125**, 237003 (2020).
- ¹⁹ W. Knafo, G. Knebel, P. Steffens, K. Kaneko, A. Rosuel, J.-P. Brison, J. Flouquet, D. Aoki, G. Lapertot, and S. Raymond, Low-dimensional antiferromagnetic fluctuations in the heavy-fermion paramagnetic ladder UTe_2 , *Phys. Rev. B* **104**, L100409 (2021).
- ²⁰ N. P. Butch, S. Ran, S. R. Saha, P. M. Neves, M. P. Zic, J. Paglione, S. Gladchenko, Q. Ye, and J. A. Rodriguez-Rivera, Symmetry of magnetic correlations in spin-triplet superconductor UTe_2 , *npj Quantum Mater.* **7**, 39 (2022).
- ²¹ H. Sakai, Y. Tokiwa, P. Opletal, M. Kimata, S. Awaji, T. Sasaki, D. Aoki, S. Kambe, Y. Tokunaga, and Y. Haga, Field Induced Multiple Superconducting Phases in UTe_2 along Hard Magnetic Axis, *Phys. Rev. Lett.* **130**, 196002 (2023).
- ²² H. Sakai, P. Opletal, Y. Tokiwa, E. Yamamoto, Y. Tokunaga, S. Kambe, and Y. Haga, Single crystal growth of superconducting UTe_2 by the molten salt flux method, *Phys. Rev. Mater.* **6**, 073401 (2022).
- ²³ A. Rosuel, C. Marcenat, G. Knebel, T. Klein, A. Pourret, N. Marquardt, Q. Niu, S. Rousseau, A. Demuer, G. Seyfarth, G. Lapertot, D. Aoki, D. Braithwaite, J. Flouquet, and J.-P. Brison, Field-induced tuning of the pairing state in a superconductor, *Phys. Rev. X* **13**, 011022 (2023).
- ²⁴ K. Machida, Theory of Spin-polarized Superconductors—An Analogue of Superfluid 3He A-phase—, *J. Phys. Soc. Jpn.* **89**, 033702 (2020).
- ²⁵ K. Machida, Notes on Multiple Superconducting Phases in UTe_2 –Third Transition–, *J. Phys. Soc. Jpn.* **89**, 0655001 (2020).
- ²⁶ K. Machida, Nonunitary triplet superconductivity tuned by field-controlled magnetization: $URhGe$, $UCoGe$, and UTe_2 , *Phys. Rev. B* **104**, 014514 (2021).
- ²⁷ K. Machida, Violation of Pauli-Clogston limit in the heavy-fermion superconductor $CeRh_2As_2$: Duality of itinerant and localized 4f electrons, *Phys. Rev. B* **106**, 184509 (2022).
- ²⁸ K. Machida, Violation of the orbital depairing limit in a nonunitary state: High-field phase in the heavy fermion superconductor UTe_2 , *Phys. Rev. B* **107**, 224512 (2023).
- ²⁹ Sylvia K. Lewin, Peter Czajka, Corey E. Frank, Gicela Saucedo Salas, Hyeok Yoon, Yun Suk Eo, Johnpierre Paglione, Andriy H. Nevidomskyy, John Singleton, and Nicholas P. Butch, High-Field Superconducting Halo in UTe_2 , arXiv:2402.18564.
- ³⁰ Hiroki Matsumura, Hiroki Fujibayashi, Katsuki Kinjo, Shunsaku Kitagawa, Kenji Ishida, Yo Tokunaga, Hironori Sakai, Shinsaku Kambe, Ai Nakamura, Yusei Shimizu, Yoshiya Homma, Dexin Li, Fuminori Honda, and Dai Aoki, Large Reduction in the a-axis Knight Shift on UTe_2 with $T_c = 2.1$ K, *J. Phys. Soc. Japan* **92**, 063701 (2023).
- ³¹ G. Nakamine, Shunsaku Kitagawa, Kenji Ishida, Yo Tokunaga, Hironori Sakai, Shinsaku Kambe, Ai Nakamura, Yusei Shimizu, Yoshiya Homma, Dexin Li, Fuminori Honda, and Dai Aoki, Superconducting properties of heavy fermion UTe_2 revealed by ^{125}Te -nuclear magnetic resonance, *J. Phys. Soc. Jpn.* **88**, 113703 (2019).
- ³² Genki Nakamine, Katsuki Kinjo, Shunsaku Kitagawa, Kenji Ishida, Yo Tokunaga, Hironori Sakai, Shinsaku Kambe, Ai Nakamura, Yusei Shimizu, Yoshiya Homma, Dexin Li, Fuminori Honda, and Dai Aoki, Inhomogeneous Superconducting State Probed by ^{125}Te NMR on UTe_2 , *J. Phys. Soc. Japan* **90**, 064709 (2021).
- ³³ Genki Nakamine, Katsuki Kinjo, Shunsaku Kitagawa, Kenji Ishida, Yo Tokunaga, Hironori Sakai, Shinsaku Kambe, Ai Nakamura, Yusei Shimizu, Yoshiya Homma, Dexin Li, Fuminori Honda, and Dai Aoki, Anisotropic response of spin susceptibility in the superconducting state of UTe_2 probed with ^{125}Te -NMR measurement, *Phys. Rev. B* **103**, L100503 (2021).
- ³⁴ Hiroki Fujibayashi, Genki Nakamine, Katsuki Kinjo, Shunsaku Kitagawa, Kenji Ishida, Yo Tokunaga, Hironori Sakai, Shinsaku Kambe, Ai Nakamura, Yusei Shimizu, Yoshiya Homma, Dexin Li, Fuminori Honda, and Dai Aoki, Superconducting Order Parameter in UTe_2 Determined by Knight Shift Measurement, *J. Phys. Soc. Jpn.* **91**, 043705 (2022).
- ³⁵ K. Kinjo, H. Fujibayashi, S. Kitagawa, K. Ishida, Y. Tokunaga, H. Sakai, S. Kambe, A. Nakamura, Y. Shimizu, Y. Homma, D. X. Li, F. Honda, D. Aoki, K. Hiraki, M. Kimata, and T. Sasaki, Change of superconducting character in UTe_2 induced by a magnetic field, *Phys. Rev. B* **107**, L060502 (2023).
- ³⁶ Katsuki Kinjo, Hiroki Fujibayashi, Hiroki Matsumura, Fumiya Hori, Shunsaku Kitagawa, Kenji Ishida, Yo Tokunaga, Hironori Sakai, Shinsaku Kambe, Ai Nakamura, Yusei Shimizu, Yoshiya Homma, Dexin Li, Fuminori Honda, and Dai Aoki, Superconducting spin reorientation in spin-

- triplet multiple superconducting phases of UTe_2 , *Sci. Adv.* **9**, eadg 2736 (2023).
- ³⁷ S. Ran, I. L. Liu, Y. S. Eo, D. J. Campbell, P. M. Neves, W. T. Fuhrman, S. R. Saha, C. Eckberg, H. Kim, D. Graf, F. Balakirev, J. Singleton, J. Paglione, and N. P. Butch, Extreme magnetic field-boosted superconductivity, *Nat. Phys.* **15**, 1250 (2019).
- ³⁸ G. Knebel, W. Knafo, A. Pourret, Q. Niu, M. Vališka, D. Braithwaite, G. Lapertot, M. Nardone, A. Zitouni, S. Mishra, I. Sheikin, G. Seyfarth, J.-P. Brison, D. Aoki, and J. Flouquet, Field-reentrant superconductivity close to a metamagnetic transition in the heavy-fermion superconductor UTe_2 , *J. Phys. Soc. Jpn.* **88**, 063707 (2019).
- ³⁹ T. Helm, M. Kimata, K. Sudo, A. Miyata, J. Stirnat, T. Förster, J. Hornung, M. König, I. Sheikin, A. Pourret, G. Lapertot, D. Aoki, J. -P. Brison, G. Knebel, and J. Wosnitza, Suppressed magnetic scattering sets conditions for the emergence of 40T high-field superconductivity in UTe_2 , arXiv:2207.08261.
- ⁴⁰ Z. Wu, T. I. Weinberger, J. Chen, A. Cabala, D. V. Chichinadze, D. Shaffer, J. Pospisil, J. Prokleska, T. Haidamak, G. Bastien, V. Sechovsky, A. J. Hickey, M. J. Mancera-Ugarte, S. Benjamin, D. E. Graf, Y. Skourski, G. G. Lonzarich, M. Valiska, F. M. Grosche, and A. G. Eaton, Enhanced triplet superconductivity in next-generation ultraclean UTe_2 , arXiv:2305.19033.
- ⁴¹ D. Aoki, K. Ishida, and J. Flouquet, Review of U-based Ferromagnetic Superconductors: Comparison between UGe_2 , $URhGe$, and $UCoGe$, *J. Phys. Soc. Jpn.* **88**, 022001 (2019).
- ⁴² A. Miyake, D. Aoki, and J. Flouquet, Pressure evolution of the ferromagnetic and field re-entrant superconductivity in $URhGe$, *J. Phys. Soc. Jpn.* **78**, 063703 (2009).
- ⁴³ D. Braithwaite, D. Aoki, J.-P. Brison, J. Flouquet, G. Knebel, A. Nakamura, and A. Pourret, Dimensionality Driven Enhancement of Ferromagnetic Superconductivity in $URhGe$, *Phys. Rev. Lett.* **120**, 037001 (2018).
- ⁴⁴ Takeshi Mizushima, Yasumasa Tsutsumi, Takuto Kawakami, Masatoshi Sato, Masanori Ichioka, and Kazushige Machida, Symmetry-Protected Topological Superfluids and Superconductors —From the Basics to 3He —, *J. Phys. Soc. Jpn.* **85**, 022001 (2016).
- ⁴⁵ Dai Aoki, Fuminori Honda, Georg Knebel, Daniel Braithwaite, Ai Nakamura, DeXin Li, Yoshiya Homma, Yusei Shimizu, Yoshiki J. Sato, Jean-Pascal Brison, and Jacques Flouquet, Multiple Superconducting Phases and Unusual Enhancement of the Upper Critical Field in UTe_2 , *J. Phys. Soc. Jpn.* **89**, 053705 (2020).
- ⁴⁶ Dai Aoki, et al, to be published.
- ⁴⁷ Georg Knebel, Motoi Kimata, Michal Vališka, Fuminori Honda, DeXin Li, Daniel Braithwaite, Gérard Lapertot, William Knafo, Alexandre Pourret, Yoshiki J. Sato, Yusei Shimizu, Takumi Kihara, Jean-Pascal Brison, Jacques Flouquet, and Dai Aoki, Anisotropy of the Upper Critical Field in the Heavy-Fermion Superconductor UTe_2 under Pressure, *J. Phys. Soc. Jpn.* **89**, 053707 (2020).
- ⁴⁸ Dai Aoki, Motoi Kimata, Yoshiki J. Sato, Georg Knebel, Fuminori Honda, Ai Nakamura, Dexin Li, Yoshiya Homma, Yusei Shimizu, William Knafo, Daniel Braithwaite, Michal Vališka, Alexandre Pourret, Jean-Pascal Brison, and Jacques Flouquet, Field-Induced Superconductivity near the Superconducting Critical Pressure in UTe_2 , *J. Phys. Soc. Jpn.* **90**, 074705 (2021).
- ⁴⁹ Wen-Chen Lin, Daniel J. Campbell, Sheng Ran, I-Lin Liu, Hyunsoo Kim, Andriy H. Nevidomskyy, David Graf, Nicholas P. Butch, and Johnpierre Paglione, Tuning magnetic confinement of spin-triplet superconductivity, *npj Quantum Mater.* **5**, 68 (2020).
- ⁵⁰ Sheng Ran, Shanta R. Saha, I-Lin Liu, David Graf, Johnpierre Paglione, and Nicholas P. Butch, Expansion of the high field-boosted superconductivity in UTe_2 under pressure, *npj Quantum Mater.* **6**, 75 (2021).
- ⁵¹ Hyunsoo Kim, I-Lin Liu, Wen-Chen Lin, Yun Suk Eo, Sheng Ran, Nicholas P. Butch, and Johnpierre Paglione, Tuning a magnetic energy scale with pressure in UTe_2 , arXiv:2307.00180.
- ⁵² Yusei Shimizu, Shunichiro Kittaka, Yohei Kono, Toshiro Sakakibara, Kazushige Machida, Ai Nakamura, Dexin Li, Yoshiya Homma, Yoshiki J. Sato, Atsushi Miyake, Minoru Yamashita, and Dai Aoki, Anomalous electromagnetic response in the spin-triplet superconductor UTe_2 , *Phys. Rev. B* **106**, 214525 (2022).
- ⁵³ Di S. Wei, David Saykin, Oliver Y. Miller, Sheng Ran, Shanta R. Saha, Daniel F. Agterberg, Jörg Schmalian, Nicholas P. Butch, Johnpierre Paglione, and Aharon Kapitulin, The interplay between magnetism and superconductivity in UTe_2 , *Phys. Rev. B* **105**, 024521 (2022).
- ⁵⁴ Lin Jiao, Zhenyu Wang, Sheng Ran, Jorge Olivares Rodriguez, Manfred Sigrist, Ziqiang Wang, Nicholas Butch, and Vidya Madhavan, Microscopic evidence for a chiral superconducting order parameter in the heavy fermion superconductor UTe_2 , *Nature*, **579**, 523 (2020).
- ⁵⁵ T. Metz, S. Bao, S. Ran, I-L. Liu, Y. S. Eo, and W. T. Fuhrman, D. F. Agterberg, S. Anlage, N. P. Butch, and J. Paglione, Point node gap structure of spin-triplet superconductor UTe_2 , *Phys. Rev. B* **100**, 220504 (R) (2019).
- ⁵⁶ Shunichiro Kittaka, Yusei Shimizu, Toshiro Sakakibara, Ai Nakamura, Dexin Li, Yoshiya Homma, Fuminori Honda, Dai Aoki, and Kazushige Machida, Orientation of point nodes and nonunitary triplet pairing tuned by the easy-axis magnetization in UTe_2 , *Phys. Rev. Research* **2**, 032014(R) (2020).
- ⁵⁷ N. Azari, M. Yakovlev, N. Rye, S. R. Dunsiger, S. Sundar, M. M. Bordelon, S. M. Thomas, J. D. Thompson, P. F. S. Rosa, and J. E. Sonier, Absence of spontaneous magnetic fields due to time-reversal symmetry breaking in bulk superconducting UTe_2 , to be published in PRL.
- ⁵⁸ K. Ishihara, M. Roppongi, M. Kobayashi, Y. Mizukami, H. Sakai, Y. Haga, K. Hashimoto, and T. Shibauchi, Chiral superconductivity in UTe_2 probed by anisotropic low-energy excitations, *Nat. Commun.* **14**, 2966 (2023)
- ⁵⁹ S. Suetsugu, M. Shimomura, M. Kamimura, T. Asaba, H. Asaeda, Y. Kosuge, Y. Sekino, S. Ikemori, Y. Kasahara, Y. Kohsaka, M. Lee, Y. Yanase, H. Sakai, P. Opletal, Y. Tokiwa, Y. Haga, and Y. Matsuda, Fully gapped pairing state in spin-triplet superconductor UTe_2 , arXiv:2306.17549.
- ⁶⁰ K. Machida and T. Ohmi, Phenomenological theory of ferromagnetic superconductivity, *Phys. Rev. Lett.* **86**, 850 (2001).
- ⁶¹ J. F. Annett, Symmetry of the order parameter for high-temperature superconductivity, *Adv. Phys.* **39**, 83 (1990).
- ⁶² Masa-aki Ozaki, Kazushige Machida, and Tetsuo Ohmi, On p-Wave Pairing Superconductivity under Cubic Symmetry, *Prog. Theor. Phys.* **74**, 221 (1985).
- ⁶³ Masa-aki Ozaki, Kazushige Machida, and Tetsuo Ohmi, On p-Wave Pairing Superconductivity under Hexagonal and Tetragonal Symmetries, *Prog. Theor. Phys.* **75**, 442

- (1986).
- ⁶⁴ Aline Ramires, Nonunitary Superconductivity in Complex Quantum Materials, *J. Phys.: Condens. Matter* **34**, 304001 (2022).
- ⁶⁵ S. Sundar, S. Gheidi, K. Akintola, A. M. Côté, S. R. Dunsiger, S. Ran, N. P. Butch, S. R. Saha, J. Paglione, and J. E. Sonier, Coexistence of ferromagnetic fluctuations and superconductivity in the actinide superconductor UTe_2 , *Phys. Rev. B* **100**, 140502 (R) (2019).
- ⁶⁶ Yo Tokunaga, Hironori Sakai, Shinsaku Kambe, Taisuke Hattori, Nonoka Higa, Genki Nakamine, Shunsaku Kitagawa, Kenji Ishida, Ai Nakamura, Yusei Shimizu, Yoshiya Homma, DeXin Li, Fuminori Honda, and Dai Aoki, ^{125}Te -NMR study on a single crystal of heavy fermion superconductor UTe_2 , *J. Phys. Soc. Jpn.* **88**, 073701 (2019).
- ⁶⁷ Yo Tokunaga, Hironori Sakai, Shinsaku Kambe, Yoshinori Haga, Yoshifumi Tokiwa, Petr Opletal, Hiroki Fujibayashi, Katsuki Kinjo, Shunsaku Kitagawa, Kenji Ishida, Ai Nakamura, Yusei Shimizu, Yoshiya Homma, Dexin Li, Fuminori Honda, and Dai Aoki, Slow Electronic Dynamics in the Paramagnetic State of UTe_2 , *J. Phys. Soc. Jpn.* **91**, 023707 (2022).
- ⁶⁸ Devi V. Ambika, Qing-Ping Ding, Khusboo Rana, Corey E. Frank, Elizabeth L. Green, Sheng Ran, Nicholas P. Butch, and Yuji Furukawa, Possible Coexistence of Antiferromagnetic and Ferromagnetic Spin Fluctuations in the Spin-triplet Superconductor UTe_2 Revealed by ^{125}Te NMR under Pressure, *Phys. Rev. B* **105**, L220403 (2022).
- ⁶⁹ Y. Tokunaga, H. Sakai, S. Kambe, P. Opletal, Y. Tokiwa, Y. Haga, S. Kitagawa, K. Ishida, D. Aoki, G. Knebel, G. Lapertot, S. Krämer, and M. Horvatić, Longitudinal spin fluctuations driving field-reinforced superconductivity in UTe_2 , *Phys. Rev. Lett.* **131**, 226503 (2023).
- ⁷⁰ G. Aeppli, E. Bucher, C. Broholm, J. K. Kjems, J. Baumann, and J. Hufnagl, Magnetic order and fluctuations in superconducting UPt_3 , *Phys. Rev. Lett.* **60**, 615 (1988).
- ⁷¹ D. Song, S. Lee, Z. Shen, W. Jung, W. Lee, S. Choi, W. Kyung, S. Jung, S. Ishida, S-R. Park, H. Eisaki, Y. Wang, K-Y. Choi, and C. Kim, Interplay between hole superconductivity and quantum critical antiferromagnetic fluctuations in electron-doped cuprates, preprint DOI:10.21203/rs.3.rs-3333329/v1.
- ⁷² P. W. Anderson, Structure of “triplet” superconducting energy gaps, *Phys. Rev. B* **30**, 4000 (1984).
- ⁷³ E. I. Blount, Symmetry properties of triplet superconductors, *Phys. Rev. B* **32**, 2935 (1985).
- ⁷⁴ G. E. Volovik, and L. P. Gor’kov, Superconducting classes in heavy-fermion systems, *Sov. Phys. JETP* **61**, 843 (1985).
- ⁷⁵ V. Ambegaokar and N. D. Mermin, Thermal anomalies of He^3 : pairing in a magnetic field, *Phys. Rev. Lett.* **30**, 81 (1973).
- ⁷⁶ K. Machida, T. Ohmi, and M. Ozaki, Anisotropy of Upper Critical Fields for d- and p-Wave Pairing Superconductivity, *J. Phys. Soc. Jpn.* **54**, 1552 (1985).
- ⁷⁷ K. Machida, M. Ozaki, and T. Ohmi, Unconventional Superconducting Class in a Heavy Fermion System UPt_3 , *J. Phys. Soc. Jpn.* **59**, 1397 (1990).
- ⁷⁸ K. Machida, T. Fujita, and T. Ohmi, Vortex Structures in an Anisotropic Pairing Superconducting State with Odd-Parity, *J. Phys. Soc. Jpn.* **62**, 680 (1993).
- ⁷⁹ K. Machida, T. Nishira, and T. Ohmi, Orbital Symmetry of a Triplet Pairing in a Heavy Fermion Superconductor UPt_3 , *J. Phys. Soc. Jpn.* **68**, 3364 (1999).
- ⁸⁰ M. Tinkham, *Introduction to Superconductivity*, McGraw-Hill, New York, 1975.
- ⁸¹ V. Jaccarino and M. Peter, Ultra-High-Field Superconductivity, *Phys. Rev. Lett.* **9**, 290 (1962).
- ⁸² A. Miyake, Y. Shimizu, Y. J. Sato, D. Li, A. Nakamura, Y. Homma, F. Honda, J. Flouquet, M. Tokunaga, and D. Aoki, Metamagnetic transition in heavy Fermion superconductor UTe_2 , *J. Phys. Soc. Jpn.* **88**, 063706 (2019).
- ⁸³ D. Aoki, private communication.
- ⁸⁴ Atsushi Miyake, Yusei Shimizu, Yoshiki J. Sato, Dexin Li, Ai Nakamura, Yoshiya Homma, Fuminori Honda, Jacques Flouquet, Masashi Tokunaga, and Dai Aoki, Enhancement and Discontinuity of Effective Mass through the First-Order Metamagnetic Transition in UTe_2 , *J. Phys. Soc. Jpn.* **90**, 103702 (2021).
- ⁸⁵ S. Takagi, Susceptibility Discontinuity at the He^3 -A: Normal Transition, *Prog. Theor. Phys.* **51**, 1998 (1974).
- ⁸⁶ D. Aoki, H. Sakai, P. Opletal, Y. Tokiwa, J. Ishizuka, Y. Yanase, H. Harima, A. Nakamura, D. Li, Y. Homma, Y. Shimizu, G. Knebel, J. Flouquet, and Y. Haga, First Observation of the de Haas-van Alphen Effect and Fermi Surfaces in the Unconventional Superconductor UTe_2 , *J. Phys. Soc. Jpn.* **91**, 083704 (2022).
- ⁸⁷ K. Miyake, Theory of Pairing Assisted Spin Polarization in Spin-Triplet Equal Spin Pairing: Origin of Extra Magnetization in Sr_2RuO_4 in Superconducting State, *J. Phys. Soc. Jpn.* **83**, 053701 (2014).
- ⁸⁸ Y. Tsutsumi and K. Machida, Topological spin texture and d-vector rotation in spin-triplet superconductors: A case of UTe_2 , arXiv:2309.02918.
- ⁸⁹ W. Knafo, T. Thebault, P. Manuel, D. D. Khalyavin, F. Orlandi, E. Ressouche, K. Beauvois, G. Lapertot, K. Kaneko, D. Aoki, D. Braithwaite, G. Knebel, and S. Raymond, Incommensurate antiferromagnetism in UTe_2 under pressure, arXiv:2311.05455.
- ⁹⁰ Sangyun Lee, Andrew J. Woods, P. F. S. Rosa, S. M. Thomas, E. D. Bauer, Shi-Zeng Lin, and R. Movshovich, Anisotropic field-induced changes in the superconducting order parameter of UTe_2 , arXiv:2310.04938.
- ⁹¹ H. Matsumura, et al, presented at the Autumn Meeting of the Japan Physical Society, September 2023.
- ⁹² K. Ishihara, M. Kobayashi, K. Imamura, M. Konczykowski, H. Sakai, P. Opletal, Y. Tokiwa, Y. Haga, K. Hashimoto, and T. Shibauchi, Anisotropic Enhancement of Lower Critical Field in Ultraclean Crystals of Spin-Triplet Superconductor UTe_2 , *Phys. Rev. Research* **5**, L022002 (2023).
- ⁹³ C. Paulsen, G. Knebel, G. Lapertot, D. Braithwaite, A. Pourret, D. Aoki, F. Hardy, J. Flouquet, and J.-P. Brison, Anomalous anisotropy of the lower critical field and Meissner effect in UTe_2 , *Phys. Rev. B* **103**, L180501 (2021).
- ⁹⁴ T. Isoshima and K. Machida, Instability of the nonvortex toward a quantized vortex in a Bose-Einstein condensate under rotation, *Phys. Rev. A* **60**, 3313 (1999).
- ⁹⁵ K. Machida, Spin Density Wave and Superconductivity in Highly Anisotropic Materials, *J. Phys. Soc. Jpn.* **50**, 2195 (1981). K. Machida and T. Matsubara, Spin Density Wave and Superconductivity in Highly Anisotropic Materials. II. Detailed Study of Phase Transitions, *J. Phys. Soc. Jpn.* **50**, 3231 (1981).
- ⁹⁶ K. Machida, K. Nokura, and T. Matsubara, Theory of antiferromagnetic superconductors, *Phys. Rev. B* **22**, 2307 (1980).
- ⁹⁷ K. Machida and H. Nakanishi, Superconductivity under

- a ferromagnetic molecular field, *Phys. Rev. B* **30**, 122 (1984).
- ⁹⁸ K. Machida and M. Kato, Inherent Spin-Density-Wave Instability in Heavy-Fermion Superconductivity, *Phys. Rev. Lett.* **58**, 1986 (1987).
- ⁹⁹ Eduardo Fradkin, Steven A. Kivelson, and John M. Tranquada, Theory of intertwined orders in high temperature superconductors, *Rev. Mod. Phys.* **87**, 457 (2015).
- ¹⁰⁰ B. Keimer, S. A. Kivelson, M. R. Norman, S. Uchida, and J. Zaanen, From quantum matter to high-temperature superconductivity in copper oxides, *Nature* **518**, 179 (2015).
- ¹⁰¹ M. Ichioka, N. Hayashi, and K. Machida, Local density of states in the vortex lattice in a type-II superconductor, *Phys. Rev. B* **55**, 6565 (1997).
- ¹⁰² Henrik S. Røising, Max Geier, Andreas Kreisel, and Brian M. Andersen, Thermodynamic transitions and topology of spin-triplet superconductivity: Application to UTe_2 , arXiv:2311.06097.
- ¹⁰³ P. Miranović, N. Nakai, M. Ichioka, and K. Machida, Orientational field dependence of low-lying excitations in the mixed state of unconventional superconductors, *Phys. Rev. B* **68**, 052501 (2003).